Mon. Not. R. Astron. Soc. **381,** 943–961 (2007) doi:10.1111/j.1365-2966.2007.12295.x

Near-infrared surface photometry of a sample of barred galaxies

D. A. Gadotti,[1,2,3⋆] E. Athanassoula,[2] L. Carrasco,[4] A. Bosma,[2] R. E. de Souza[1] and E. Recillas[4]

[1]*Departamento de Astronomia, Universidade de São Paulo, Rua do Matão 1226, 05508-090 São Paulo-SP, Brasil*
[2]*Laboratoire d'Astrophysique de Marseille, Observatoire Astronomique de Marseille Provence, 2 Place Le Verrier, 13248 Marseille Cedex 04, France*
[3]*Max-Planck-Institut für Astrophysik, Karl-Schwarzschild-Strasse 1, D-85748 Garching bei München, Germany*
[4]*Instituto Nacional de Astrofísica, Optica, y Electrónica, Luis Enrique Erro 1, Tonantzintla, CP 72840, Puebla, Mexico*

Accepted 2007 July 30. Received 2007 June 20; in original form 2007 February 9

ABSTRACT

We have obtained deep J and K_s images of a sample of nine barred galaxies in order to collect a reliable and homogeneous set of images to which N-body simulations of barred galaxies will be compared. The observations were performed using the new near-infrared camera available at the 2.1-m telescope of the Observatorio Astrofísico Guillermo Haro (OAGH) in Cananea, Sonora, Mexico. We present the results of surface photometry techniques applied to the observed images, as well as to the deprojected images. These results include radial profiles of surface brightness (elliptically averaged), colour, position angle, ellipticity and the b_4 Fourier component. In addition, we present isophotal maps, colour maps, surface brightness profiles along the bar major and minor axes, characteristic radial scalelengths and bar length estimates. We discuss how projection effects can influence these measurements and the uncertainties introduced by deprojecting galaxy images. We show that analytical expressions can be used to obtain reliable estimates of deprojected bar lengths, ellipticities and position angles directly from the observed images. These expressions are based on the assumption that the outer parts of the bar are vertically thin, as shown by theoretical work. The usefulness of our data in addressing issues on bar formation and evolution is also discussed. In particular, we present results showing a steep drop in the ellipticity profile, as expected for bar formation processes in which the dark matter halo plays a fundamental role. Furthermore, we show that the location of this drop is a good indicator of the end of the bar in strongly barred galaxies, as predicted by numerical models.

Key words: galaxies: evolution – galaxies: formation – galaxies: fundamental parameters – galaxies: haloes – galaxies: photometry – galaxies: structure.

1 INTRODUCTION

It is now widely recognized that bars are one of the major drivers of galaxy evolution and play a crucial role in shaping the present properties of galaxies (see Kormendy & Kennicutt 2004; Athanassoula 2005a, for recent reviews of the observational and theoretical aspects). Comprehensive studies, both observational and theoretical, are therefore called for to allow us to understand best these structures. Furthermore, a strong connection between bars and the dark matter haloes hosting disc galaxies was recently revealed. Athanassoula (2003, 2002) showed that a significant exchange of angular momentum between near-resonant particles in the disc and in the dark halo leads to stronger bars. Thus, at least in principle, the observed properties of real bars may give us information on the ability of the halo and of its resonances to absorb angular momentum from the inner disc and, thus, indirectly, some clues on halo properties, like its mass and velocity distributions. In Athanassoula & Misiriotis (2002, hereafter AM02) the model with an initially centrally concentrated halo (their model Massive Halo; MH) develops a bar which is much stronger, longer and thinner than the bar in their Massive Disc (MD) model, that has a less initially centrally concentrated halo. A Fourier analysis of the face-on density distribution of model MH shows that the non-axisymmetric components are very large compared to those of model MD. Moreover, also the shape of the halo is linked to the evolution of the bar. Numerical simulations have shown that an initially spherical halo evolves in shape and becomes prolate-like in the central parts, as the galaxy forms a strong bar, and rotates with the same pattern speed as the bar (Athanassoula 2005a,c; Colin, Valenzuela & Klypin 2006; Athanassoula 2007). Curir & Mazzei (1999), Gadotti & de Souza (2003) and Heller, Shlosman & Athanassoula (2007) suggest that

⋆E-mail: dimitri@mpa-garching.mpg.de

non-axisymmetric haloes could trigger the bar instability. In particular, Heller et al. (2007) stress that thus the bar formation timescale could be very short. On the other hand, the bar growth at later stages of the evolution can be severely compromised by a non-axisymmetric halo (El-Zant & Shlosman 2002; Berentzen, Shlosman & Jogee 2006; Heller, Shlosman & Athanassoula 2007). Many intricacies in the bar–halo connection are as yet not fully understood. However, since triaxial haloes are predicted by cosmology models in which galaxies form through hierarchical merging (e.g. Cole & Lacey 1996; Hayashi, Navarro & Springel 2007), the observed properties of bars may eventually lead to clues concerning the very first assembling of galaxies.

Hence, one might devise methods to indirectly derive the physical properties of dark matter haloes from the observed properties of the bars they host. The first step in such a study would be, however, to check how well present bar models describe real bars. If the models are successful, then they might indeed give us useful estimates of the true physical properties of real haloes, via comparisons of observations of barred galaxies to models with known halo properties. Hence, a detailed comparison between the structural properties of real galactic bars and those arising in *N*-body simulations of barred galaxies is necessary. The first challenge in the pursuit of such a comparison is to convene an appropriate set of galaxy images. For a reliable comparison with *N*-body models, these images must comply with certain criteria. Ideally, they should be deep and in the near-infrared (NIR) wavelength, so that a given galaxy image is a true representation of the bulk of its stellar population. This is a fundamental point since the overall evolution of an *N*-body simulation is driven by the gravitational potential created by the model as a whole. Evidently, such a sample of galaxy images would also benefit from a homogeneous treatment, that simplifies the interpretation of the results. In this respect, the Two-Micron All-Sky Survey (2MASS) (see http://www.ipac.caltech.edu/2mass/) is advantageous on a statistical level.

Menendez-Delmestre et al. (2007) measured the bar fraction and the relative sizes of bars and discs using 2MASS images of 151 nearby spiral galaxies. In another recent NIR study on bars, based this time on the OSUBSGS, Marinova & Jogee (2007) made a similar analysis based on 180 spirals and found that most bars have moderate to high ellipticity. The main aim of these studies is to provide a reference for comparisons with galaxies at higher redshifts. Our aim is totally different; we want to provide a sample for detailed comparison of observations to *N*-body simulations. We therefore opted for a much smaller sample, and made a detailed analysis based on individual studies and an inspection of each case. The importance of this for our specific purposes will be made clear during this work. For the same reasons we aimed at obtaining deeper images.

In this paper, we describe an effort to acquire a suitable set of deep NIR images of barred galaxies which will be used to study the morphological properties of bars and of their host galaxies. With these images, ellipse fits are possible down to isophote levels $\approx$1 mag fainter, on average, than the detection limit in 2MASS images, both in J and K_s. To achieve this depth, we had to limit our sample size. Furthermore, we avoid relying on automated procedures. Instead, we do the analysis for each galaxy individually, examine each case separately and assess all the results by eye. This is generally not feasible if the sample contains many galaxies. Here, we present results based mostly on ellipse fits, and postpone to a future paper the analysis of Fourier components and bar strength (e.g. Laurikainen et al. 2004; Buta et al. 2005, 2006).

Our images were obtained with the NIR camera of the 2.1-m telescope of the Observatorio Astrofísico Guillermo Haro (OAGH) in Cananea, Mexico. The observatory is operated by the Instituto Nacional de Astrofísica, Optica, y Electrónica (INAOE) and details about the Cananea Near-Infrared Camera (CANICA) will be presented in L. Carrasco et al. (in preparation). The general properties of the galaxies in our sample and the steps taken in the observations and data reduction are described in Sections 2 and 3, respectively. Applying surface photometry techniques, we determine many physical properties of the bars and of the galaxies, which are presented in Section 4 and discussed in detail in Section 5. Section 6 deals specifically with bar length measurements. In Section 7, we briefly discuss features and uncertainties in deprojected galaxy images and the use of these data to assess whether, and up to what extent, results of up-to-date *N*-body simulations of barred galaxies agree with the photometric observations. We summarize and conclude in Section 8.

2 THE SAMPLE

Our sample consists of nine galaxies whose relevant properties are given in Table 1. All of them were observed in J and K_s. Since we aimed for deep NIR imaging, we have not looked for a complete, unbiased sample, but instead we chose suitable galaxies for our scientific goals, namely a comparison to *N*-body simulations of barred galaxies. Our target galaxies also had to comply with the apparent size limit imposed by the undistorted field of view of the camera ($\approx$3 arcmin – see Section 3), since we wanted to avoid doing time-consuming mosaics. All galaxies are local, most are bright, many relatively close to face-on and they span a range in morphologies. According to de Vaucouleurs et al. (1991, hereafter RC3), three are weakly barred (SAB) and six are strongly barred (SB). Six galaxies have morphological types S0 or S0/a and the remaining three go as late type as Sb. Table 1 also shows that four galaxies in our sample have nuclei with non-stellar activity [active galactic nuclei (AGN)].

The choice of local, bright and moderately inclined galaxies gives us more reliable estimates for the structural parameters of these galaxies, since it means higher signal-to-noise ratio (S/N) and higher spatial resolution, while in more edge-on systems a proper description of some bar properties may be unattainable. Because deprojected measurements are preferred for a suitable comparison of real images to *N*-body realizations, we avoided highly inclined systems. This assures us that spurious geometric effects introduced by image deprojection techniques are avoided for most of our galaxies.

The diversity of our sample might be helpful in trying to evaluate clues related, for instance, to the prominence of the classical bulge and the bar strength. The presence of galaxies with AGN might also be relevant to help in understanding the role played by bars in the fuelling of such nuclei. We also note that, except for NGC 799, no galaxy in our sample is part of a pair, or of a multiple system, which means that their bars are most likely fully due to internal instabilities, with no significant help from tidal forces. This assessment was made using the Lyon Extragalactic Data Archive (LEDA) and publicly available images in the NASA/IPAC Extragalactic Database (NED), but does not exclude the possibility that these galaxies are members of galaxy clusters. NGC 799 has an interacting companion similar in size and luminosity at a projected distance of the order of its own diameter. There are, however, no signs of a violent interaction, which suggests that it might be in an early stage, or that the passage may be retrograde, or the deprojected separation is much larger than the projected one.

Table 1. Properties of the sample galaxies.

Galaxy	Type	M_B	m_B	cz (km s^{-1})	Distance (Mpc)	$D_{25}/2$ (arcmin)	Inclination (°)	PA_{ln} (°)	$PA_{ln} - PA_{bar}$ (°)	AGN
(1)	(2)	(3)	(4)	(5)	(6)	(7)	(8)	(9)	(10)	(11)
NGC 266	SB(rs)ab	−22.0	12.6	4770	68.1	1.5	13.7	150	50	···
NGC 357	SB(r)0/a	−20.2	13.1	2379	34.0	1.1	44.9	20	80	LINER
NGC 799	(R')SB(s)a	−20.7	14.1	5846	83.5	1.0	34.4	100	55	···
NGC 1211	(R)SB(r)0/a	−20.1	13.5	3132	44.7	0.9	46.2	30	60	···
NGC 1358	SAB(r)0/a	−20.9	13.2	3924	56.1	1.1	53.6	15	60	Sey2
NGC 1638	SAB(rs)0^o?	−20.5	13.1	3209	45.8	1.1	55.9	70	4	···
NGC 7080	SB(r)b	−21.4	13.6	4998	71.4	0.9	19.6	0	75	···
NGC 7280	SAB(r)0^+	−19.4	13.1	1942	27.7	1.0	54.4	78	12	AGN
NGC 7743	(R)SB(s)0^+	−19.7	12.6	1725	24.6	1.4	31.0	80	−20	Sey2

Notes. Column (1) identifies the galaxy and column (2) gives its morphological type according to RC3. Columns (3) and (4) show, respectively, the absolute and apparent *B*-band magnitude, according to LEDA. In column (5), the LEDA radial velocity in km s^{-1}, corrected for the infall of the Local Group towards Virgo, is displayed, and the galaxy distance in Mpc, using $H_0 = 70$ km s^{-1} Mpc^{-1}, appears in column (6). Column (7) shows the radius of the 25 *B*-band mag arcsec^{-2} isophote according to LEDA, in arcminutes. Column (8) gives the inclination angle of the plane of the galaxy to the plane of the sky, in degrees, as in LEDA, except for NGC 7743 to which this parameter was derived in Section 4.4. The position angle of the line of nodes (from the north to the east) and the difference between this position angle and that of the bar, that is, the parameter α in our analytical treatments, are shown in columns (9) and (10), respectively, in degrees (see Section 6 for details). Finally, column (11) shows the AGN designation as given in NED.

3 OBSERVATIONS AND DATA REDUCTION

The NIR images of the galaxies in our sample were obtained with CANICA, a camera based on a HAWAII 1024 × 1024 pixel array, available at the 2.1-m telescope of the OAGH, in Mexico. The plate scale and field of view are 0.32 arcsec pixel^{-1} and about 5.5 × 5.5 arcmin^2, respectively (note, however, that the outskirts of the field of view suffer from optical distortions, meaning that, for our purposes, the safest procedure is to avoid galaxies larger than approximately 3 arcmin in diameter). An electronic cross-talk effect is present in CANICA at a 0.9 per cent level, which might cause photometric errors if there are bright sources in a given field. This means that, if there is a bright star in the field of the galaxy, a very small fraction of the star light can be spread through a few consecutive lines in the array and, in some cases, cross the galaxy image. Unfortunately, this happened to the images of two of our galaxies. Although the effect may be negligible, we took all the necessary steps so that our results are not affected and we present the corresponding procedures at the end of this section.

The data were obtained during a single run of 12 nights in 2004 September and October, when all galaxies were observed in both J and K_s. Table 2 shows relevant data on the observing run. Except for four nights possibly with small clouds, most of the nights were clear and photometric. This made our photometric measurements quite accurate. Every night, several standard stars from Hunt et al. (1998) were observed in both bands. The photometric error for each night was assumed to be the standard deviation between our estimated magnitude and the magnitude determined in Hunt et al. (1998) for the standard stars observed. This means that, since during some nights there were more stars observed than in others, the error estimates have different accuracies. This may explain why the error in the photometric nights is typically not too different from that in the non-photometric nights. The mean zero-point error in J in the photometric nights is 0.06 mag, reaching 0.08 mag in the non-photometric nights. Similarly, in K_s we have errors of 0.08 and 0.10 mag, respectively. Coincidentally, in the non-photometric nights we had a full moon increasing the sky brightness, but that in fact does not seem to harm our measurements, as expected for NIR observations. We lost, however, some images due to the direct incidence of moon light in the dome. As expected, the error estimates show that the photometric accuracy is generally higher in J than in K_s.

Table 2. Summary of the observations.

Night	Galaxy	Photometric?	Error (J)	Error (K_s)
22/09	N7280;N1211Ks	Yes	0.05	0.06
23/09	N7280J;N7743Ks;N1211Ks	Yes	0.11	0.14
24/09	N7743J;N1211J	Yes	0.06	0.10
25/09	N7080Ks;N1358Ks	No	0.06	0.12
26/09	N7080Ks;N1358	No	0.06	0.09
27/09	N7080;N1358J;N1638Ks	No	0.07	0.05
28/09	N7080J;N1638	No	0.13	0.15
30/09	N7080J;N1638J	Yes	0.05	0.07
01/10	N357	Yes	0.06	0.06
02/10	N266Ks;N357J	Yes	0.01	0.11
03/10	N266J;N799Ks	Yes	0.06	0.04
04/10	N799	Yes	0.10	0.10

Notes. For each night, we list the galaxies observed with the corresponding band appended to the name of the galaxy; when no band information is given, images in both bands were taken. Photometric errors are given in magnitudes.

We note that our average errors in the photometric zero-point are 0.07 mag in J and 0.09 mag in K_s, which is quite good for NIR bands.

Our observations, nevertheless, have one drawback, namely the seeing, which was poor during the whole run. The full width at half-maximum (FWHM) of Gaussian fits to the light profile of standard stars observed in the J band was constantly around 2.0 arcsec. Moreover, after co-adding all images taken for a given galaxy in a given band the spatial resolution got poorer by typically 0.5 arcsec, due to uncertainties in the process of combining many images. All galaxies were observed during two or more nights to reach the total integration time aimed for, and also sometimes to replace images that were found to have problems, such as due to a bad telescope move or when the galaxy image was out of the undistorted field of view of the camera.

Using results from previous NIR observations (Gadotti & de Souza 2003, 2006), we designed an observing strategy in order to reach an S/N of ∼3 at the 21 K_s mag arcsec^{-2} isophote, although we could not be very precise since technical parameters like the camera efficiency were not known, because the data obtained as part of its commissioning were not fully reduced and analysed. Currently,

CANICA's technical details can be found in the OAGH web pages. Nevertheless, the ellipse fits to the isophotes of our images described further below reach on average $20.1 \pm 1.1\,K_s$ mag arcsec^{-2} and 21.4 ± 1.2 J mag arcsec^{-2}. To reach this S/N we needed a total exposure time on target of 6000 s per galaxy per band, which was in fact achieved. In a few cases, the total integration time is a bit smaller due to problems in some images.

Since NIR images are limited by background emission, we used the following observing strategy. We define as a cycle a set of 18 exposures of 50 s each, starting with two consecutive exposures on target, followed by two on sky and so on. In K_s, we ran 12 such cycles per galaxy. The interwoven sky exposures are necessary for a proper background subtraction, since the background intensity can change significantly in time-scales as short as a few minutes. As it can also change rapidly spatially, the sky images were taken only a few arcminutes from the galaxy. The sky images are dithered a few arcseconds in order to ease the removal of unwanted objects. Similarly, we dithered the galaxy images in order to avoid the effects of bad pixels. Since the sky background is fainter and more stable in J, the individual exposures in this band reach 150 s, so that only four cycles per galaxy were needed. For the standard stars, the background contribution can be well estimated within the star image frame and typically we made eight dithered images of around 10 s each to get the final star image.

Before actually going through all data-reduction steps, *every* image was checked for problems, even though the number of image files is very large (72 per galaxy in J, 216 per galaxy in K_s). For the treatment of the images, we used the GEMINI IRAF[1] package. Flat-field images were obtained through the QFLAT task from combining many dome images. We decided to use dome flat-fields, instead of flat images obtained from sky images, after checking with many standard stars that the former produced more accurate results in terms of photometry (i.e. smaller zero-point errors). The QSKY task was used to estimate the background contribution. For each galaxy image, the background was estimated from the four sky images closest in time. Furthermore, the mean and standard deviations of every sky image were calculated, and if the mean was discrepant from that of the other three sky images by more than 10 per cent of the standard deviation then the image was removed from the process. In this way, we avoid background changes and ensure a proper background subtraction. Interestingly enough, the standard deviation of the sky images was very similar even when there were (small) changes in the mean, and typically only a few background images had to be removed per galaxy. These corrections (flat-fielding and background subtraction) were performed for every galaxy and standard star image by QREDUCE, using the appropriate flat-field and background images. Finally, the IMCOADD task combines by the median all corrected images of a galaxy, calculating the necessary shifts due to the dither pattern.

In an effort to avoid spurious effects caused by the electronic cross-talk mentioned above, the J and K_s images of NGC 1358 and NGC 7743 (in this study, the only galaxies whose images are affected by this problem) underwent further processing. This consisted of the following steps. First, the lines of the detector having the problem were identified (by visually inspecting the images) and masked out. Next, using the ELLIPSE and BMODEL tasks in IRAF, a simple model image was fitted to the galaxy. The ellipse fits were performed in a similar way to those presented below. Finally, the bad lines were substituted by the corresponding lines from the model.

[1] IRAF is distributed by the National Optical Astronomy Observatories, which are operated by the Association of Universities for Research in Astronomy, Inc., under cooperative agreement with the National Science Foundation.

4 SURFACE PHOTOMETRY ANALYSIS

4.1 General presentation

Fig. 1 shows for each galaxy the J-band direct image, as well as $J - K_s$ colour maps with J-band isophotal contours overlaid (with a difference of 0.5 mag between two consecutive contours). The latter were built by dividing the J image by the K_s image (both in analog digital number units) after trimming and alignment. Since the point spread function (PSF) FWHM is very similar in both bands, there was no need for degrading the PSF of any of the images. The grey-scales in these figures vary from galaxy to galaxy since they were chosen to emphasize each galaxy's main features. These figures show clearly the deepness of our images, witnessed, for instance, by the fact that one is able to trace the spiral arms (e.g. in NGC 266) for quite a large azimuthal angle, which is not usual in the NIR. A similar evaluation can be done from the data in Table 1 and Figs 3–11 below, as well as from a comparison with images from 2MASS in NED.

Fig. 2 shows the surface brightness profiles along the major and minor axes of the bars of the galaxies in our sample. Most of the profiles along the bar major axis show the typical shoulders found in optical images for bars (especially strong ones) in galaxies with morphological types earlier than Sbc (Elmegreen & Elmegreen 1985).

We fitted ellipses to the isophotes of each galaxy in both bands, using the IRAF task ELLIPSE. The increase in the semimajor axis between two consecutive isophote fits is 1 pixel (0.32 arcsec). We thus built radial profiles of the elliptically averaged surface brightness, and of geometric parameters of the isophotes, namely position angle, ellipticity and the b_4 Fourier coefficient. These geometric parameters are practically identical in the two bands so we just show (Figs 3–11) those relative to the J band, where the S/N is better. In addition, we present $J - K_s$ colour profiles.

4.2 Ellipse fitting

During the ellipse-fitting procedure the centre was held fixed. To find the galaxy centre, we first ran ELLIPSE with the centre free and then chose as centre a typical value from those given by the task for the isophotes at a radius around 10–15 pixels. We found that the dispersion of the values of the central coordinates obtained from this region is generally lower (i.e. only 1–2 pixels) than the corresponding dispersion at larger radii. In addition, this region is far enough from the centre to make sure that poor statistics do not result in an ill-defined centre. After fixing the centre, the error bars given by ELLIPSE for the coordinates of the centre are of the order of 1 pixel. Similar results are obtained for both the x- and y-coordinates. Interestingly, the location of the galaxy centre determined in this way is often identical to that of its brightest pixel (and when it is not, the differences are below 1–2 pixel). Similar results are obtained using the IMCENTROID task in IRAF.

One may ask whether different results could arise from the ellipse fits if the centre was left free. To check that, we inspected the ellipse fits to the J-band image of NGC 266, when letting the central coordinates vary. It turned out that the results do not change significantly over most of the galaxy. The position of the centre of each isophote varies only by a few pixels, which does not cause substantial changes in the other relevant radial profiles. When one reaches the outer spiral arms, however, the central coordinates might assume

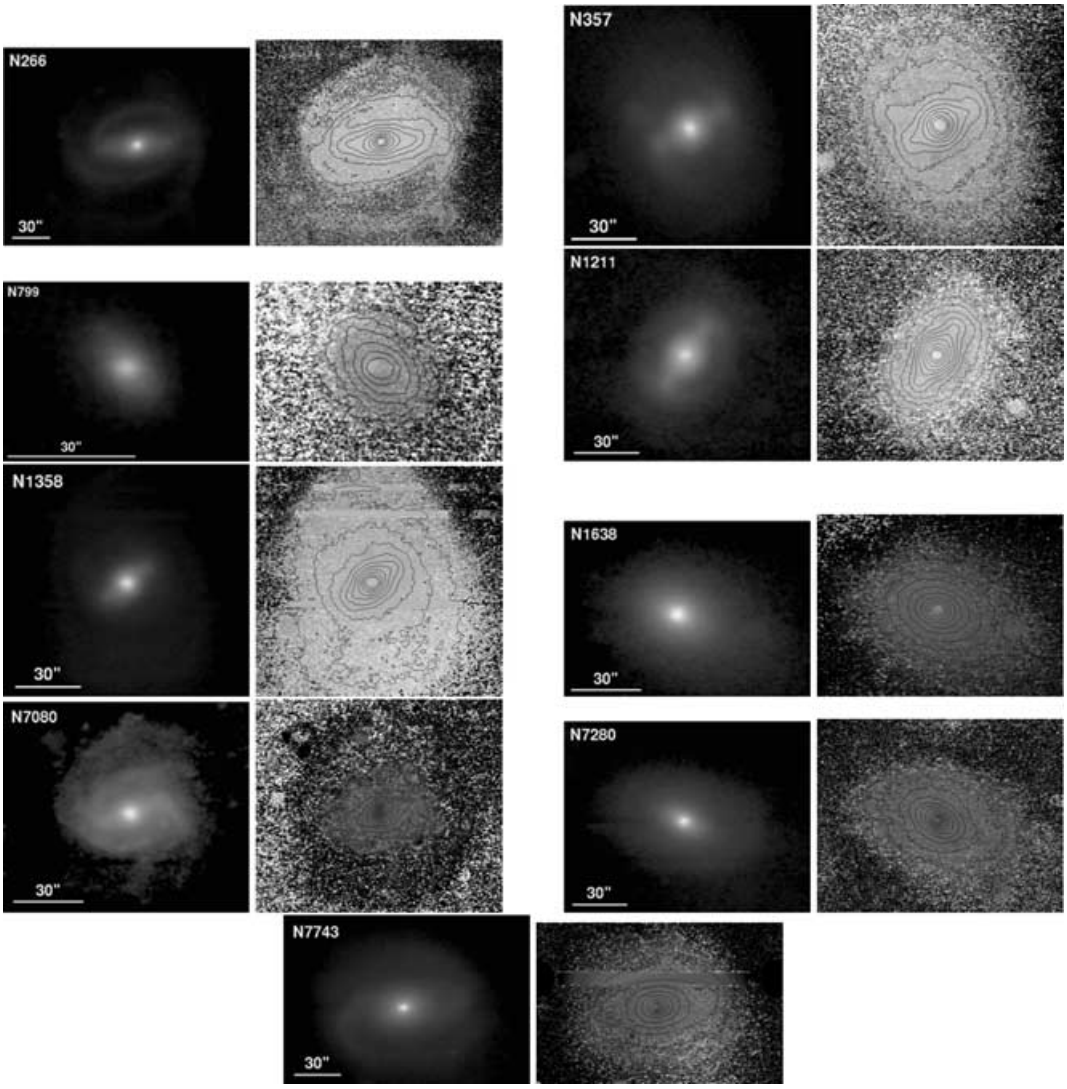

Figure 1. *J*-band images (left-hand panel) and $J - K_s$ colour maps (right-hand panel) of the galaxies in our sample. Colour maps have *J*-band isophotal contours overlaid and are coded so that redder features are darker. The north is up, and the east is to the left-hand side.

completely wrong values, by as much as several tens of pixels, and thus will of course affect all radial profiles in this region. This is due to the asymmetric nature of the arms. We thus always held the centre fixed in the ellipse fits presented here.

The ellipticity of an isophote is defined as $1 - b/a$, where a and b are, respectively, the semimajor and semiminor axes of the best-fitting ellipse. The b_4 coefficient is related to the fourth harmonic term of the Fourier series that fits the deviations of the isophote from a pure ellipse (Jedrzejewski 1987; see also the IRAF help pages). It is the amplitude that multiplies the term cos (4θ) normalized by the isophote semimajor axis length and the local intensity gradient (where θ is the azimuthal angle). This coefficient thus measures deviations from a pure ellipse that are due to either boxy ($b_4 < 0$) or discy ($b_4 > 0$) isophotes. Edge-on bars produce boxy isophotes (e.g. de Souza & dos Anjos 1987; Kuijken & Merrifield 1995; Bureau & Freeman 1999; Bureau & Athanassoula 2005, and references therein). In face-on barred galaxies, the superposition of the bar and a prominent classical bulge may create discy isophotes (see de Souza, Gadotti & dos Anjos 2004; Gadotti & de Souza 2006; Athanassoula et al. 1990, and the results below). If, however, the bulge component is carefully masked out, then, at least for SB early-type galaxies, the isophotes have a strong rectangular-like shape (Athanassoula et al. 1990). This argues that the intrinsic shape of bar isophotes is in fact rectangular-like, while the discy outlines are due to the superposition of the bulge component. This argument is further strengthened by ellipse fits to *N*-body bars (AM02), where the classical bulge component can be easily removed and fits can be made to the disc only, or to the disc plus bulge components.

Similarly, the a_4 coefficient is the amplitude of the sin (4θ) term. It is important to stress that to measure the strength of the $m = 4$ Fourier component in the galaxy image one has to account for the contribution of both terms. This is always done when a_4 and b_4 are measured using circular concentric rings (see e.g. Ohta et al. 1990; AM02; Buta et al. 2006; Laurikainen et al. 2006), but is neglected when they are measured from ellipse fitting. Indeed, in the latter case it is implicitly assumed that the $m = 2$ and 4 components have roughly the same position angle. If this is true, one expects a_4 to be negligible, since the fitted ellipses will be aligned with the bar in the bar region. We checked this assumption for our sample and found that it holds for five galaxies: in the bar region, the maximum of a_4

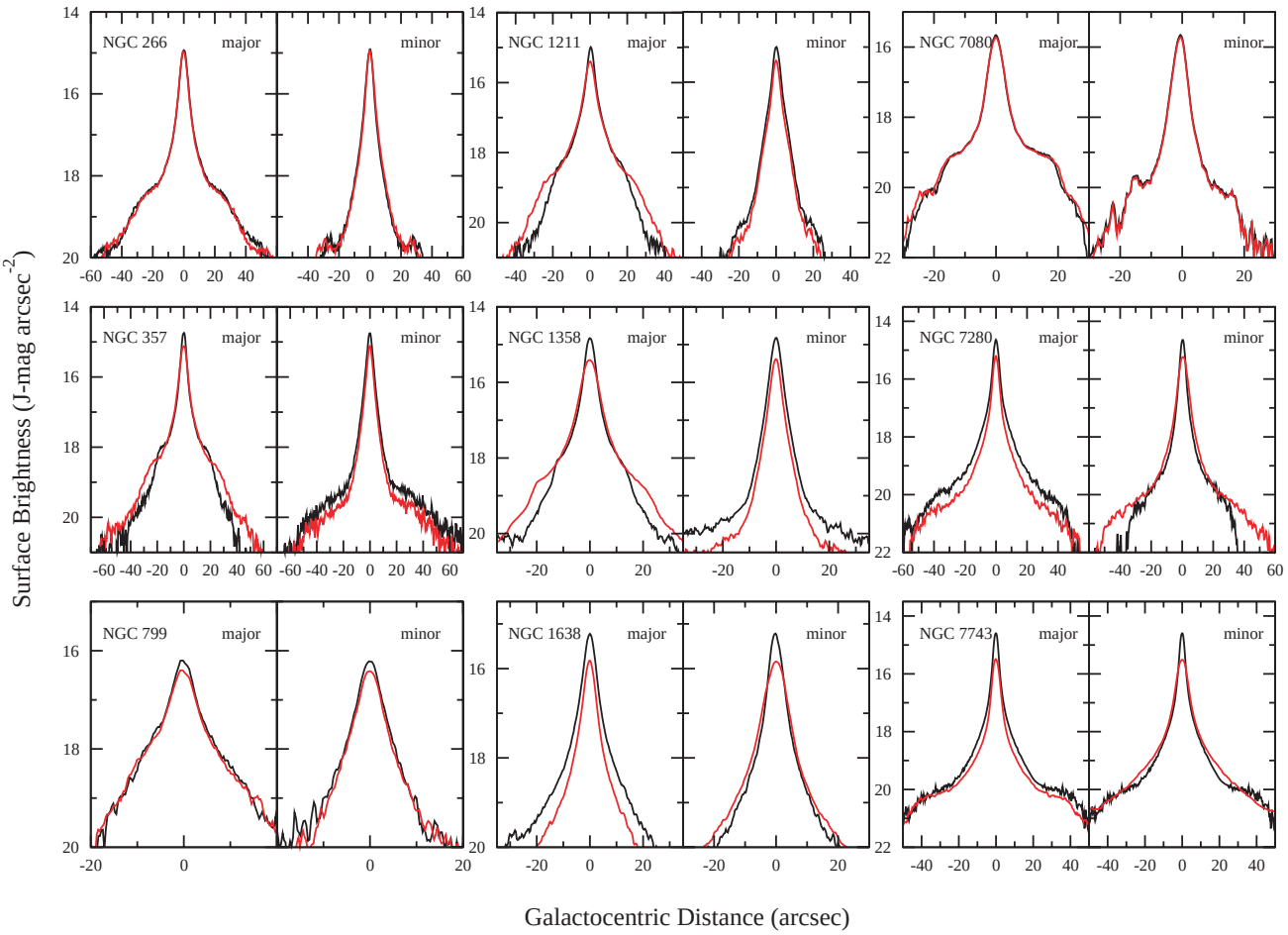

Figure 2. *J*-band surface brightness profiles along the bar major and minor axes for the galaxies in our sample. The red lines refer to deprojected images.

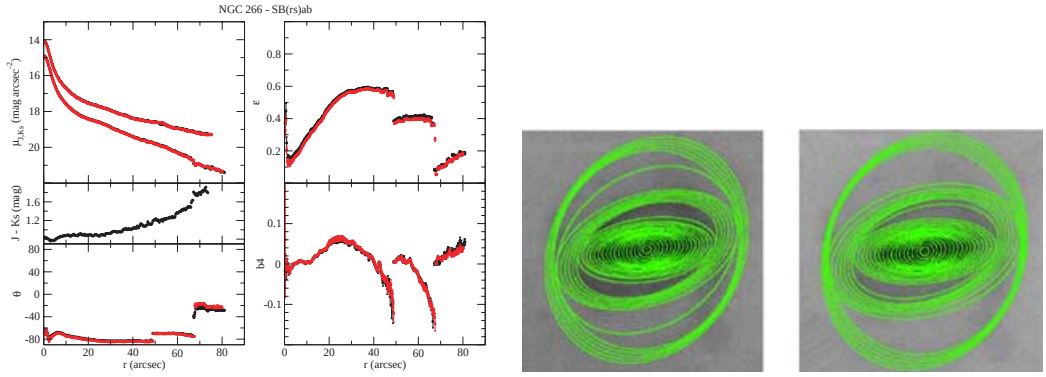

Figure 3. Radial profiles resulting from the ellipse fitting to the isophotes of NGC 266. Top left-hand panel: surface brightness in *J* and K_s. Bottom left-hand panel: position angle (from the north to the east). Top right-hand panel: ellipticity. Bottom right-hand panel: the b_4 Fourier coefficient. Middle left-hand panel: J− K_s colour. The red points correspond to the analysis on deprojected images. *J*-band images of the galaxy correspond to direct (left-hand panel) and deprojected (right-hand panel) views and have a fraction of the ellipse fits overlaid.

is much smaller than that of b_4 (smaller by a factor of 5, or more). However, for NGC 266, 357, 7080 and NGC 7743, the ratio of the a_4 peak to the b_4 peak is, respectively, 0.04/0.06, 0.04/0.12, 0.03/0.14 and 0.02/0.04. Hence, the contribution from a_4 can be as large as half that of b_4, even when these parameters are estimated through ellipse fits, rather than using circular concentric rings. Interestingly, we note that all galaxies with a significant contribution from a_4 have conspicuous spiral arms or rings, which might contribute to the $m = 2$ and 4 differently from the bar. These results show that it can be hazardous to straightforwardly neglect the contribution of the a_4 component.

4.3 Comments on individual galaxies

Our images of NGC 357, NGC 1211 and NGC 7280 reach the 25 *B*-band mag arcsec^{-2} isophote. On the other hand, in the cases of

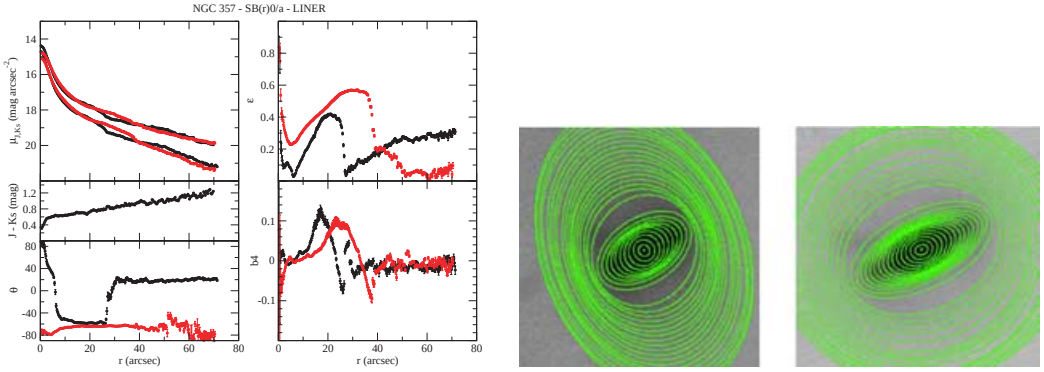

Figure 4. Same as Fig. 3 but for NGC 357.

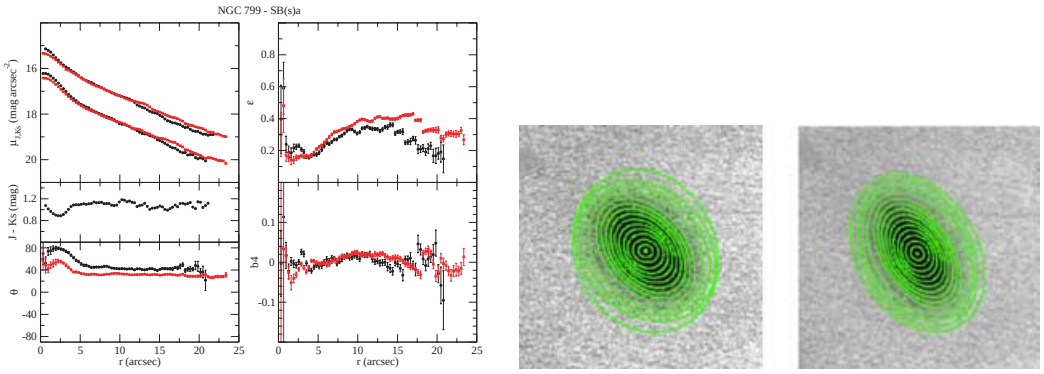

Figure 5. Same as Fig. 3 but for NGC 799.

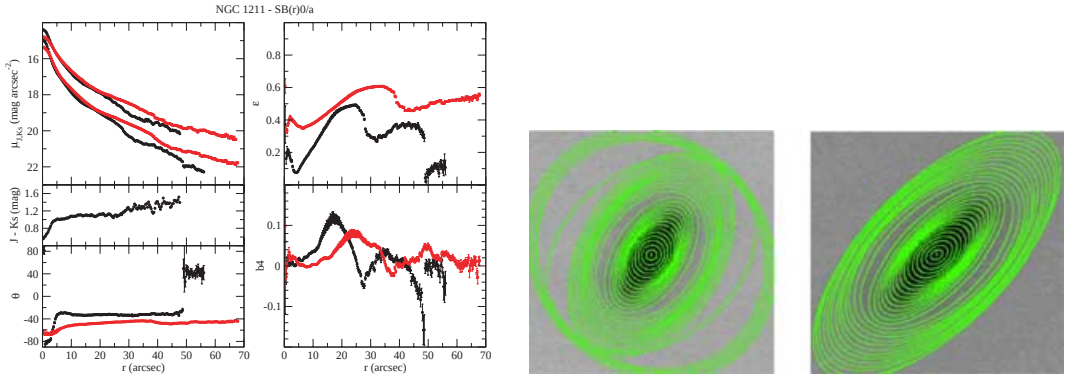

Figure 6. Same as Fig. 3 but for NGC 1211.

NGC 799 and NGC 1358 our surface photometry analysis goes approximately only half as far. For the former, a Sloan Digital Sky Survey image (SDSS – http://www.sdss.org) shows that the bar is relatively weak and is embedded in a lens. It is interesting to note that Erwin & Sparke (2003) found a secondary bar in NGC 7280, which is likely the cause of the first peak we find in its ellipticity profile in the nuclear region (at ≈1 arcsec from the centre – Fig. 10). In addition, Erwin & Sparke (2002) comment that NGC 7743 has a nuclear spiral structure which stands out clearly as a blue feature in the colour map and colour profile we present here (Figs 1 and 11, respectively). In this case too, this might be the cause of the ellipticity peak we find in the nuclear region (≈1–2 arcsec). Note, however, that seeing effects are important at these distances from the centre in all our images.

The isophotal contours of NGC 1638 display a considerable asymmetry which seems to be real, and not an artifact from wrong sky subtraction, since it is also present in the images available in NED. The origin of this asymmetry might be related to the presence of dusty spirals over the north-east corner of the galaxy.

In the images and colour maps of NGC 1358 and NGC 7743, it is possible to identify the detector lines corrected by the electronic leak problem discussed previously, and whose correcting procedure is presented in Section 3. The changes introduced by these corrections in the original galaxy image are not in terms of brightness or brightness gradient, but in the absence of noise. This was verified by analysing intensity cuts parallel and perpendicular to the corrected lines, as well as along them. This is due to the fact that these lines were generated by a model which does not include noise. Since

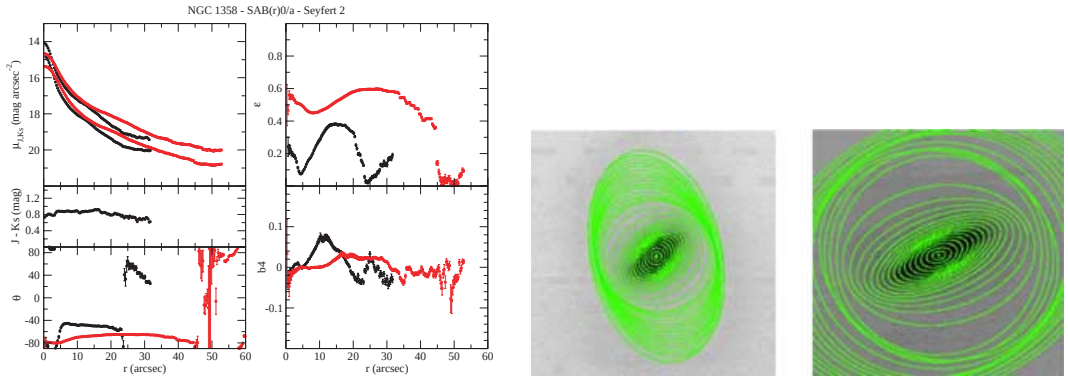

Figure 7. Same as Fig. 3 but for NGC 1358.

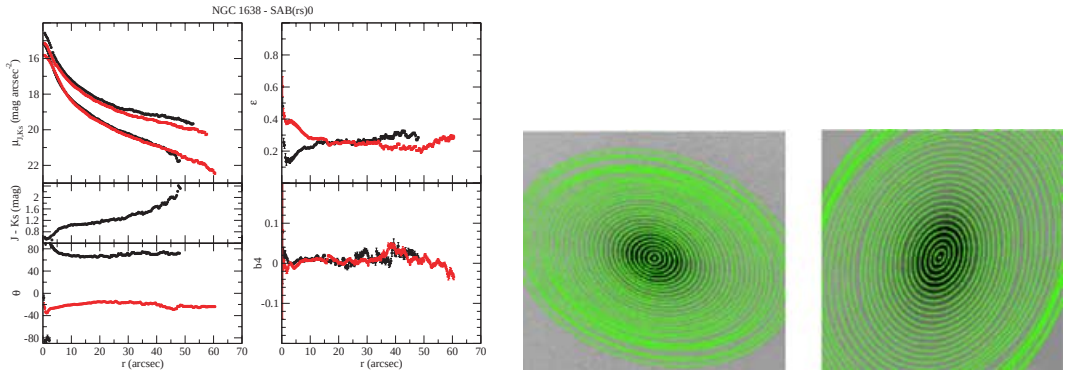

Figure 8. Same as Fig. 3 but for NGC 1638.

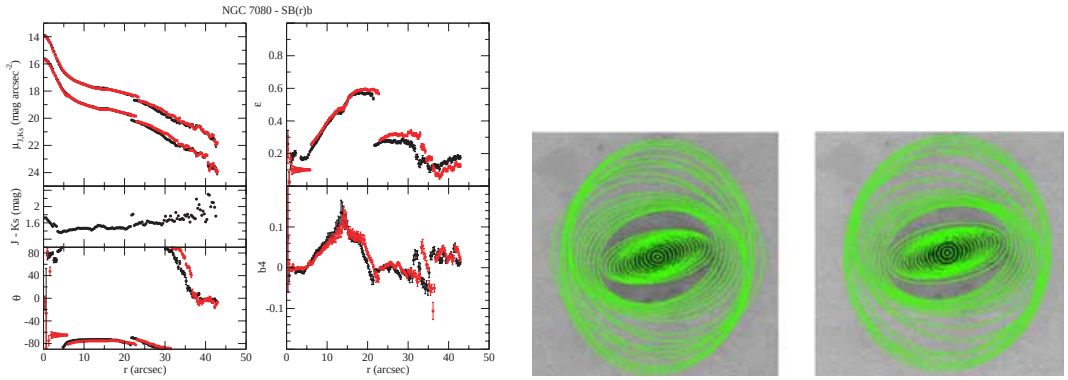

Figure 9. Same as Fig. 3 but for NGC 7080.

the brightness range in the colour maps is very narrow (only a few tenths of magnitude), this difference in the corrected lines stands out more clearly in these maps than in the direct images. Nevertheless, it is important to stress that, since the correction was generated by models from ellipse fitting, this problem does not introduce spurious effects to the results presented in this paper, which are themselves based on ellipse fits to the galaxy images.

4.4 Deprojecting the images

The surface photometry techniques applied to the observed images were also applied to deprojected images of all galaxies in our sample (results shown in red in Figs 2–11). To deproject each galaxy image, we performed a flux-conserving stretching of the direct images in the direction perpendicular to the line of nodes, using the IRAF task IMLINTRAN. As the position angle of the line of nodes (PA_{ln}), we adopted that of the 25 mag arcsec^{-2} isophote in the *B*-band from RC3, except for NGC 266, 357, 1358 and NGC 7080. For these galaxies this information is not present in RC3, and so we considered the position angle of our faintest isophote fit. The inclination angles *i* were taken from LEDA, except for NGC 7743 (see below). Since errors in the estimates of PA_{ln} and *i* can lead to wrong results when deprojecting galaxy images, it is important to check whether our values agree with those of other sources, when available. For PA_{ln}, we checked estimates from LEDA and a visual inspection of deep blue and red images from the Second Generation

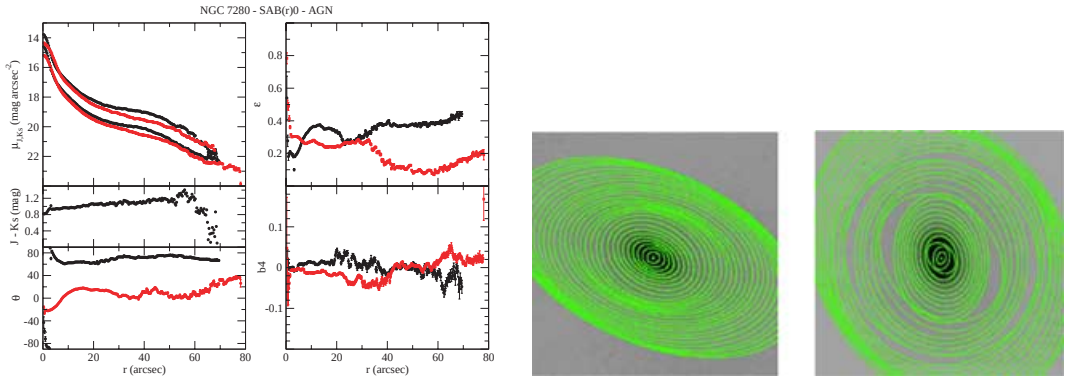

Figure 10. Same as Fig. 3 but for NGC 7280.

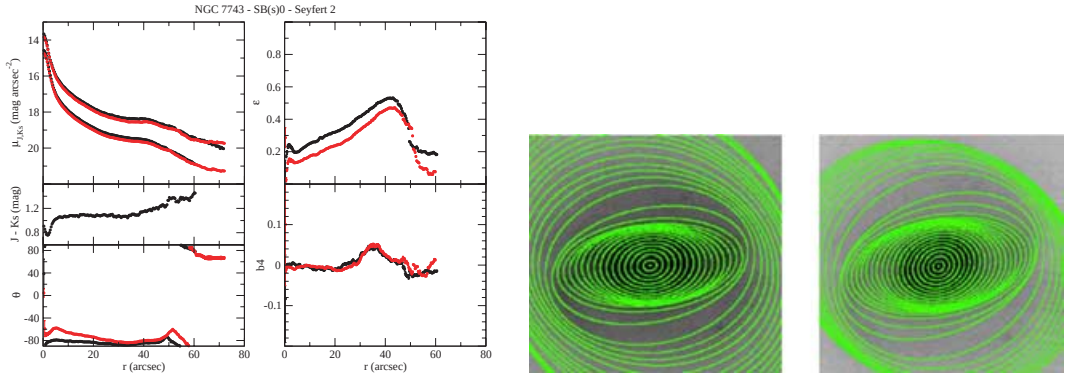

Figure 11. Same as Fig. 3 but for NGC 7743.

Digitized Sky Survey (DSS2), available, for example, at SKYVIEW (http://skyview.gsfc.nasa.gov). For NGC 799 and NGC 1211, we also inspected images from SDSS. All estimates agree within $\approx 10^\circ$ except for NGC 266, NGC 1358 and NGC 7080. For NGC 1358, the position angle from LEDA is 49°, while the estimates both from our images and from the DSS2 images point to 15°. We stick to our estimates and suggest that the LEDA value results from shallower images, as one can conclude from Fig. 7, where one sees that 49° is the position angle of the isophotes at about 27 arcsec, going to 15° farther away from the centre. Likewise, the PA_{ln} values of NGC 266 and NGC 7080 quoted in LEDA (95° and 100°, respectively) are significantly different from the estimates both from our images and from the DSS2 images. These values, however, were determined from the shallower images of the 2MASS and clearly refer to an inner part of the galaxies, as can be checked through a visual inspection of the images and from the results of our ellipse fits in Figs 3 and 9.

It is also possible to use the DSS2 and SDSS images to measure the axial ratio of the outer isophotes and to obtain another estimate for i, assuming that the outer disc should be intrinsically circular. For most of our galaxies, these estimates agree with those from LEDA, with a difference of less than about 20°. The two exceptions are NGC 266, which appears to be more inclined in the DSS2 images, and NGC 7743, which appears to be less inclined. For NGC 266, since Ma, Peng & Gu (1998) give an angle very similar to LEDA (12°.2) we adopted the LEDA estimate. For NGC 7743, we obtained from the DSS2 images an axial ratio $b/a = 0.85$, resulting in an inclination angle of $\approx 31^\circ$. This is a factor of 2 lower than the value quoted in LEDA. We decided to discard the LEDA value and use our estimate for the inclination angle of this galaxy since it agrees with the value quoted in Erwin (2005). We found in the literature a different source for the inclination angle of two other galaxies in our sample. For NGC 357, Erwin (2004) gives a somewhat lower inclination (37°), but still within 10° from the LEDA value. For NGC 7280, Erwin (2005) gives an angle of 48°, again similar to the LEDA value. Table 1 lists our adopted values for PA_{ln} and i.

5 RADIAL PROFILES

5.1 Surface brightness radial profiles

In this paper, we present three different types of photometric radial profiles. In Fig. 2, we show those along the major and minor axes of the bars. They were built by extracting intensity counts from the images along two narrow strips, each over one of the bar axes. The position angle of the bar major axis, PA_{bar}, was estimated from the ellipse fits to the isophotes in the bar region (see Figs 3–11). The strips have a width of 5 pixels, over which an average is calculated to obtain the final intensity value at a given galactocentric distance. Evidently, the contribution of the bar is maximized in the luminosity profile along its major axis, making this type of profile especially suitable to study bars. The disc contribution is only clearly seen after the end of the bar, especially in the case of a strong bar. This means that to make a better assessment of the disc component in such a

case one has to look at the luminosity profile along the bar minor axis, where the contribution of the bar is minimized.

In Figs 3–11, we show surface brightness radial profiles obtained from the ellipse fits. The intensity at each point is an azimuthal average over the fitted ellipse and its galactocentric distance is the length of the ellipse semimajor axis. Note that the ellipticities and position angles of the fitted ellipses vary. This means, for instance, that these luminosity profiles are *not* calculated over a straight path from the centre to the outskirts of the galaxy. Thus, although the contributions from each individual galaxy component are added together in this type of luminosity profile, such a profile is still very useful, since it depicts the major component in the different regions of a galaxy. For barred disc galaxies like those studied here, it is clear that while bulge and disc dominate the inner and outer parts, respectively, bars can be the dominant component at intermediate distances from the centre.

NIR imaging is not optimum for studying the outermost part of discs. However, inspecting the surface brightness profiles along the bar minor axis in Fig. 2 one notes that for all galaxies in our sample the disc can be suitably described with a pure exponential law (Freeman 1970) until the limits of our measurements. The bulge contribution in the inner part is also clearly seen in all galaxies, regardless of the type of luminosity profile.

Although the drops associated with the end of the bar are easier to detect in the luminosity profiles along the bar major axis in Fig. 2, they are also present in many of the elliptically averaged profiles in Figs 3–11 (see NGC 357, 1211, 1358 and NGC 7080). This suggests the use of these drops to measure bar lengths, which will be discussed further below, since these drops are due to the smaller amount of light coming from outside the bar region. It is interesting to note how all luminosity profiles change in the deprojected images (especially, of course, for the more inclined galaxies). In particular, when the bar position angle is not close to the position angle of the line of nodes, bars can get longer when deprojected. Thus, the location of the drops associated with the end of the bar can change when the images are deprojected. Interestingly, the slope of the profile after these drops can get less steep as a result of the image stretching.

5.2 Ellipticity radial profiles

In almost all cases, the ellipticity profiles display a clear systematic behaviour and follow a well-defined pattern. Let us consider first those from the observed (projected) images. After the nuclear region, for which we cannot draw any firm conclusion due to insufficient resolution, the ellipticity increases steadily, often quasi-linearly, from 0.1–0.2 to a high value (0.4–0.6), and then stays nearly constant forming a plateau. In NGC 7743, the extent of this plateau is very small, but in other cases it is considerable. For example, in NGC 1211 it is around 8 arcsec (1.7 kpc). The extent of this region is largest in NGC 266, where it is 23 arcsec (7.6 kpc). After this plateau there is a steep drop, as one would expect from a very sharp transition between an elongated component (e.g. a bar) and a near-circular component (e.g. a ring or a disc). In some of our galaxies, like NGC 266 and NGC 7080, this drop is so steep that we have no isophotal fits in the corresponding very narrow radial extent. After this steep drop the ellipticity increases again, but to a smaller value, which is a function of the inclination and intrinsic ellipticity of the disc. Three galaxies clearly deviate from this pattern: NGC 799, NGC 1638 and NGC 7280. They will be discussed further below.

A similar clearly defined pattern is seen in the ellipticity profiles of the simulations of AM02 (we refer the reader particularly to their fig. 4). MH-type models display a plateau in the ellipticity values followed by a very sharp drop, as observed in most of our galaxies. AM02 used the location of this drop as one of the possible ways to measure the end of their MH-type bars. On the other hand, in MD-type models the decrease in ellipticity with radius is much more gradual.

Two of our galaxies, NGC 266 and NGC 7080 (and to a lesser extent also NGC 1211), have a second plateau at radii larger than the first one. It is interesting to note that these galaxies are those exhibiting the sharpest drops after the first plateau. A careful analysis of the images and the corresponding isophotal ellipse fits suggests that these plateaus are caused by a second component, also non-axisymmetric but not as much as the bar. We hesitate to call these components a lens, because their extent is longer than that of the bar, contrary to what was found by Kormendy (1979) for lenses. We will, lacking a better term, call them oval discs. They are just outside the bar, where the stellar orbits are expected to be less eccentric (Athanassoula 1992; Patsis, Skokos & Athanassoula 2003) and they have a somewhat different position angle than that of the bar (except in NGC 1211). A *B*-band image of NGC 266 shows no clear lens, and argues that this oval disc is surrounded by the inner spiral arms, while the optical SDSS image of NGC 1211 shows an inner ring/lens at a position similar to that of the second plateau, a feature absent in our NIR images. The second ellipticity plateau in NGC 7080 may be influenced by the spiral arms, since the position angle of this second structure varies somewhat with radius in a smooth way, as is generally expected for spiral arms. Note, however, that the position angle of the isophotes that describe its spiral arms and outer disc changes much faster. In these three galaxies, there is a second steep drop in ellipticity after the oval disc (this drop is less sharp in NGC 7080). After the second drop, the ellipticity follows the general trend found in the outer parts of the other galaxies, increasing steadily to a small value that reflects the disc inclination and intrinsic ellipticity.

The deprojected ellipticity radial profiles show a very similar pattern, although, as expected, the ellipticity values and the position of the plateau/peak might change. NGC 357 is a nice example of these changes: the bar becomes longer and more eccentric when deprojected, whereas the outer disc becomes more circular, as expected (see Fig. 4). A notable exception is NGC 1211, which shows more eccentric outer isophotes in the deprojected image. There is a clear explanation, however: the fit does not reach the outer, rounder disc present in the direct image, but rather goes up only to the second ellipticity plateau, caused by the oval disc (see Fig. 6).

NGC 7743 is a more ambivalent case. The plateau is of very short extent and reaches, in the deprojected case, a relatively small value ($\approx$0.4), considerably smaller than that of the other, clear MH-type bars, whose maximum deprojected ellipticity is, in all cases, about 0.6. Furthermore, a closer inspection of the images and ellipse fits of NGC 7743 (Figs 1 and 11) reveals that the peak in the ellipticity profile and the corresponding steep drop are not caused by the bar, as in the cases discussed above, but by the inner parts of the outer spirals arms. All these arguments taken together lead us to classify NGC 7743 as an MD-type bar, rather than an MH one. It could also be an intermediate case. In MH types, a considerable amount of angular momentum is exchanged within the galaxy, emitted by the inner disc and absorbed by the halo and the outer disc. In MD types, less angular momentum is exchanged. NGC 7743 could be an intermediate type, with an intermediate amount of angular momentum exchanged.

As already mentioned, three other galaxies decidedly deviate from the clear pattern of MH-type galaxies, namely NGC 799, NGC 1638

and NGC 7280. Note that these three galaxies have a maximum in the deprojected ellipticity smaller than that occurring in the other galaxies. NGC 799 has a plateau of a very short extent, followed by a gradual decrease in ellipticity, rather than by a steep drop as for the galaxies we discussed above. As we already noted, the latter property is characteristic of MD-type galaxies (AM02). Unfortunately, our surface photometry for this galaxy does not reach very deep (see Section 4.3), but a comparison to other images available in NED reveals that our images miss the faint and blue spiral arms in the outer disc. Nevertheless, Figs 1, 2 and 5 argue strongly for an MD-type bar. In particular, in the region where the position angle of the isophotes stays constant, the ellipticity first increases and then decreases steadily, a clear signature of an MD-type bar. NGC 7280 also has a drop in ellipticity clearly less sharp than those occurring in the MH-type bars, and our images for this galaxy are amongst our deepest ones. Again, the bar is evident in the ellipse fits (see Figs 1 and 10).

NGC 1638 is a less clear case. It shows just a big plateau at a relatively low ellipticity value, with no clear drop. Such a behaviour could be observed in a barred galaxy if the ellipse fits did not go beyond the end of the bar. Since our fits reach 50 arcsec, and 21.5 and 19.5 mag arcsec^{-2} in the J and K_s images, respectively, this is rather unlikely. We are more inclined to believe that NGC 1638 is truly *not* barred. In fact, the classification from RC3, SAB(rs)0°?, means there is a lot of uncertainty, and no sign of a bar can be seen either on the images or on the surface brightness profiles. The value of the ellipticity is relatively low and the position angle and b_4 profiles also do not show any clear sign of a bar. We checked optical and NIR images available in NED and also found no sign of a bar. A search in the literature reveals that the revised Shapley–Ames catalogue (Sandage & Tammann 1981) considers this galaxy as unbarred, which is not very surprising, since these authors were less compelled to classify a galaxy as barred, in particular as SAB, than the classifiers in RC3 (see Gadotti 2003). Furthermore, Ebneter, Davis & Djorgovski (1988) also found no sign of a bar. We thus conclude that out of the four galaxies which are not MH type, one is unbarred, two are clearly of MD type and the remaining one is either MD or intermediate.

5.3 The b_4 radial profiles

A systematic behaviour in the b_4 radial profiles (projected and deprojected) is also clearly apparent for most of our galaxies. These profiles generally have small values for the inner roughly 10 arcsec, rise due to the bar, and then fall to negative values and finish close to zero. The values of b_4 become negative (indicating boxy isophotes) roughly at the radius where the ellipticity reaches the plateau or maximum, or slightly after that. This occurs in the outermost region of the bar where the influence from the bulge is minimum, and thus also argues in favour of a rectangular-like shape for bars. In addition, the minimum in b_4 (i.e. the maximum boxyness) in our MH-type galaxies occurs at a larger distance from the centre than the ellipticity peak, arguing that this peak gives only a lower limit for the bar length of MH-type bars. Interestingly enough, the minimum in b_4 is located at the same position as the steep drop in ellipticity (see above), and so this is another argument in favour of using the location of this drop as a characteristic scalelength and to compare it to the bar length, at least for MH-type bars. NGC 266 shows an interesting behaviour that happens repeatedly in the ellipticity, b_4 and position angle profiles. One sees three distinct regions with the same boundaries in the three profiles. The first region clearly corresponds to the bar, the second to the oval disc/inner spiral arms just outside the bar (discussed above), and the third to the outer disc. This can also be assessed through optical images. To a lesser extent, this is also seen in NGC 1211 and NGC 7080. On the other hand, NGC 799, NGC 7280 and NGC 7743 have the least prominent values of b_4 and, interestingly enough, *these are also the bars with the lowest ellipticity maxima*. This holds for both projected and deprojected measurements and reinforces our suggestion that NGC 799, NGC 7280 and NGC 7743 are indeed real cases of MD bars. To fully establish this point, in a future paper we will perform Fourier decomposition of the galaxies in our sample, since MH and MD bars have also distinct signatures in this kind of analysis, as mentioned above. The various differences between MH and MD bars are discussed at length in AM02, including edge-on morphology and kinematics.

5.4 Colour profiles

The colour profiles in Figs 3–11 were built from the ellipse fits in each band separately. This is justified since the relevant geometrical properties of the fitted ellipses are generally identical in both bands, meaning that light from different regions of the galaxy is not mixed. A careful inspection of these profiles reveals varied behaviours. NGC 799 and NGC 1358 present a fairly flat, or slightly negative, global colour gradient (bluer outwards). On the other hand, NGC 357, NGC 1638 and NGC 7280 have positive global colour gradients (redder outwards), although the slope in the latter is small. NGC 266, 1211, 7080 and NGC 7743 show an inner flat colour profile with a significant reddening after a certain radius. While the inner parts of these colour profiles are well estimated, we cannot rule out the possibility that a difficult sky subtraction, in particular in the K_s band, is the reason behind at least some of the outer red colours. Even considering all our efforts for a good sky subtraction, this is not a trivial task, especially when pushing to faint brightness levels in the NIR. We have not found any relation of this feature with the presence of the moon or non-photometric nights. To be on a safe side, it is better to consider the observed sudden outward reddening as spurious.

With the exception of NGC 7080, all galaxies have nuclei that are bluer than their immediate surroundings, and many times the nucleus is the bluest part of the galaxy (see also the colour maps in Fig. 1). This does not seem to be strictly related to AGN activity, although this connection is difficult to analyse since we do not have information on AGN activity for all our galaxies (see Table 1). As pointed out by Gadotti & dos Anjos (2001), these colour variations probably reflect changes in the *age* of the stellar population. In particular, the blue nuclei observed here are likely to be the result of starbursts fuelled by secular processes induced by the bars. Apart from the outer and innermost regions, the colour profiles are generally quite flat.

6 CHARACTERISTIC SCALELENGTHS RELATED TO THE BAR SIZE

6.1 Bar lengths from projected and deprojected images

Measuring the bar length is not a trivial problem, as thoroughly discussed by Erwin (2005) and by AM02 for bars in real galaxies and in N-body simulations, respectively. A further discussion of the ways to measure the length of N-body bars has been given by O'Neill & Dubinski (2003), Michel-Dansac & Wozniak (2006) and Martinez-Valpuesta, Shlosman & Heller (2006). AM02 introduced seven different characteristic scalelengths and discussed their use for

measuring the bar lengths in MH- and MD-type bars. Here, we will broadly follow their lead, since our ultimate goal is a comparison of observed and *N*-body bars. We will thus adopt four out of their seven measures and add three more. It should be noted that there are small differences between the ways the measurements are made in the observations and in the simulations, but they are deemed negligible for the purposes of our comparisons.

The phase angle of the $m = 2$ Fourier component should be constant in the bar region and so we can measure the bar-length, $L_{\rm phase}$, from the position where the phase angle changes abruptly at the transition between the bar and the outer disc (or another component such as a ring, or spiral arms). In practice, we will determine the radius at which the position angle of the fitted ellipses changes by more than 10° from that of the bar. The latter is defined as the average position angle of the ellipse fits to the isophotes in the bar region, that is, the region within which no significant change ($>10^\circ$) in the position angle radial profile occurs (see Figs 3–11). Ten degrees is a usually chosen, yet arbitrary, threshold, that results in fair estimates in most cases.

From the ellipticity profiles, we can obtain three characteristic scalelengths linked to the bar. Namely, the position of the maximum ellipticity, $L_{\epsilon_{\rm max}}$ ($L_{b/a}$ in AM02), the position of the steep drop in ellipticity, $L_{\rm drop}$ (more precisely, the last position before the maximum change in slope in the ellipticity profile just after $L_{\epsilon_{\rm max}}$), and the position of the first ellipticity minimum outside the bar's maximum ellipticity, $L_{\epsilon_{\rm min}}$. This last characteristic length was not included in those used in AM02, but has been later introduced and found useful (Erwin & Sparke 2003; Erwin 2005). As already discussed in AM02, for galaxies of the MH type, whose ellipticity profile has a plateau, the measure $L_{\epsilon_{\rm max}}$ is neither meaningful nor useful, since there is no significant difference in ellipticity to distinguish one point of the plateau from another. Similarly, $L_{\rm drop}$ is not meaningful for galaxies of the MD type, since their ellipticity profile has no steep drop. Finally, $L_{\epsilon_{\rm min}}$ should be roughly the same as $L_{\rm drop}$ in the MH-type galaxies, since they have a steep drop.

A further measure of the bar-length can be obtained from the surface brightness profiles. Usually, the end of the bar is taken as the end of the flat ledge, due to the bar, along the bar major axis profile (see Fig. 2). We will call this scalelength $L_{{\rm prof}_i}$. However, one can also define the end of the bar as the position where the drop after the flat ledge in the brightness profile joins up to the disc. We will show below that the latter definition generally gives better estimates, and we will call it $L_{{\rm prof}_f}$. As already discussed in AM02, these measurements cannot be applied to MD-type galaxies, since these do not have a ledge in the photometric profiles. Furthermore, sometimes these measurements are difficult to obtain, even for MH-type bars, if the ledge is not clearly defined. In particular, $L_{{\rm prof}_f}$ is usually more difficult to obtain than $L_{{\rm prof}_i}$, demanding a higher S/N. In some cases, it could only be clearly defined in the elliptically averaged profiles in Figs 3–11. Nevertheless, we find that, for the cases where these measurements can be applied, the mean difference between the measurements at the two opposite sides of the bar is only about 1–2 per cent.

To these scalelengths we will add yet another one, obtained from the b_4 radial profiles, namely the position of the b_4 peak, L_{b_4}. Since b_4 should be positive in the regions where the bulge contribution is important and negative outside it, we expect L_{b_4} to be smaller than the bar-length.

Note that any of the scalelengths mentioned might fail to reveal the true length of the bar in certain cases. For instance, if the bar is smoothly connected with another component, such as a lens or spiral arms, with a similar position angle or ellipticity, parameters like $L_{\rm phase}$ or $L_{\epsilon_{\rm max}}$ can be significantly larger than the length of the bar. Inspecting the images is thus a mandatory safety check, especially for galaxies with a complex morphology.

We measured these characteristic scalelengths for all our galaxies and give the results for the projected and deprojected images in Tables 3 and 4, respectively. We give the results both in arcsec, so as to allow comparisons with Figs 1–11, and in kpc, to allow comparisons between different galaxies and with previous work. In Sections 5.2 and 5.3, we discussed the existence of a second separate substructure in the ellipticity and b_4 radial profiles of NGC 266, NGC 1211 and NGC 7080, presumably due to a lens-like or oval disc component. We measured the characteristic scalelengths of these substructures too and include the results in Tables 3 and 4, under the entries NGC 266b, NGC 1211b and NGC 7080b, respectively.

Note that, as expected, some of the measurements are just not doable. For instance, one cannot rigorously define $L_{\rm drop}$ in the MD-type bar of NGC 799. Furthermore, $L_{\epsilon_{\rm max}}$ in MH-type galaxies like NGC 266 does not represent true peaks in ellipticity, but just the position in the ellipticity plateau that happens to have a

Table 3. Estimates for bar-lengths from direct images in arcsec (left-hand side) and kpc (right-hand side).

Galaxy	$L_{\epsilon_{\rm max}}$	$L_{\rm drop}$	$L_{\epsilon_{\rm min}}$	$L_{\rm phase}$ (arcsec)	L_{b_4}	$L_{{\rm prof}_i}$	$L_{{\rm prof}_f}$	$L_{\epsilon_{\rm max}}$	$L_{\rm drop}$	$L_{\epsilon_{\rm min}}$	$L_{\rm phase}$ (kpc)	L_{b_4}	$L_{{\rm prof}_i}$	$L_{{\rm prof}_f}$
N266	37.9	49.1	49.1	48.5	25.2	30.6	35.0	12.5	16.2	16.2	16.0	8.3	10.1	11.6
N266b	63.0	66.0	67.0	67.0	53.0	···	···	20.8	21.8	22.1	22.1	17.5	···	···
N357	21.2	24.8	27.3	26.7	17.0	18.8	23.3	3.5	4.1	4.5	4.4	2.8	3.1	3.8
N799	14.1	···	21.0	21.0	11.1	···	···	5.7	···	8.5	8.5	4.5	···	···
N1211	24.9	28.1	31.8	48.4	17.1	18.9	30.0	5.4	6.1	6.9	10.5	3.7	4.1	6.5
N1211b	42.9	48.8	48.8	48.8	35.0	···	···	9.3	10.6	10.6	10.6	7.6	···	···
N1358	15.1	23.0	24.2	23.2	11.0	12.9	15.4	4.1	6.2	6.6	6.3	3.0	3.5	4.2
N7080	17.9	22.0	22.0	21.4	13.9	17.9	20.1	6.2	7.6	7.6	7.4	4.8	6.2	7.0
N7080b	28.9	32.1	35.0	26.0	26.0	23.1	···	10.0	11.1	12.1	9.0	9.0	8.0	···
N7280	14.2	20.9	23.1	32.1	···	···	···	1.9	2.8	3.1	4.3	···	···	···
N7743	42.9	45.4	57.1	47.9	36.1	40.3	···	5.1	5.4	6.8	5.7	4.3	4.8	···

Notes. Bar-length estimates for each galaxy: $L_{\epsilon_{\rm max}}$ is the position of the maximum of the ellipticity profile; $L_{\rm drop}$ is the last position before the maximum change in slope in the ellipticity profile just after $L_{\epsilon_{\rm max}}$; $L_{\epsilon_{\rm min}}$ is the position of the first ellipticity minimum after $L_{\epsilon_{\rm max}}$; $L_{\rm phase}$ is the position where the position angle of the isophotes changes by more than 10° from that of the bar; L_{b_4} is the position of the maximum in b_4 and, finally, in the last two columns we give the length estimates from the luminosity profile, $L_{{\rm prof}_i}$ and $L_{{\rm prof}_f}$ (see the text for further details). In some cases no reliable estimate was possible. Estimates for the second substructure in NGC 266, 1211 and NGC 7080 are also given (see the text for details).

Table 4. Estimates for bar-lengths from deprojected images in arcsec (left-hand side) and kpc (right-hand side).

Galaxy	$L_{\epsilon_{\max}}$	$L_{\rm drop}$	$L_{\epsilon_{\min}}$	$L_{\rm phase}$ (arcsec)	L_{b_4}	$L_{{\rm prof}_i}$	$L_{{\rm prof}_f}$	$L_{\epsilon_{\max}}$	$L_{\rm drop}$	$L_{\epsilon_{\min}}$	$L_{\rm phase}$ (kpc)	L_{b_4}	$L_{{\rm prof}_i}$	$L_{{\rm prof}_f}$
N266	41.8	49.1	49.1	49.1	23.6	30.1	35.0	13.8	16.2	16.2	16.2	7.8	10.2	11.9
N266b	62.1	67.0	67.9	67.9	53.0	···	···	20.5	22.1	22.4	22.4	17.5	···	···
N357	31.5	35.8	38.8	50.9	23.6	23.0	38.2	5.2	5.9	6.4	8.4	3.9	3.8	6.3
N799	17.0	···	23.0	(23.0)	9.9	···	···	6.9	···	9.3	(9.3)	4.0	···	···
N1211	34.1	37.8	42.4	(67.7)	23.5	24.0	41.0	7.4	8.2	9.2	(14.7)	5.1	5.2	8.9
N1211b	67.7	···	···	···	49.8	···	···	14.7	···	···	···	10.8	···	···
N1358	24.6	44.9	47.8	44.9	16.9	21.0	24.6	6.7	12.2	13.0	12.2	4.6	5.7	6.7
N7080	16.5	22.8	22.8	23.1	14.2	17.3	22.1	6.7	7.9	7.9	8.0	4.9	6.0	7.7
N7080b	30.9	32.9	38.2	28.0	28.0	25.1	···	10.7	11.4	13.2	9.7	9.7	8.7	···
N7280	28.4	32.8	50.0	29.9	···	···	···	3.8	4.4	6.7	4.0	···	···	···
N7743	44.0	47.1	57.9	48.7	37.2	41.3	···	5.2	5.6	6.9	5.8	4.4	4.9	···

Notes. The same as Table 3 but for the deprojected images. The values in parentheses for $L_{\rm phase}$ come from the assumption that our photometric measurements reach just this point.

slightly larger value. Some measurements might be complicated in the deprojected images. While in the direct images of NGC 799 and NGC 1211 $L_{\rm phase}$ is clearly defined, it is not in the corresponding deprojected images. In NGC 799, the change in the position angle of the ellipse fits in the direct image is small and might have been just smeared out in the deprojection of the image. In NGC 1211, since the inclination angle is relatively large, $L_{\rm phase}$ is pushed to the limits of the image, as mentioned in Section 5.2. For both galaxies, we assume that the deprojected radial profiles just reach $L_{\rm phase}$ and the corresponding values are put within parenthesis in Table 4. Comparing the profiles of the projected and deprojected images (Figs 5 and 6) shows that this is a reasonable assumption. For instance, the ratio of $L_{\epsilon_{\max}}$ in the deprojected and direct images is of the same order as the corresponding ratio for $L_{\rm phase}$ if one uses our assumption.

The position angle threshold in the definition of $L_{\rm phase}$ is another issue. If the position angles of the bar and the component just outside it are roughly the same, then $L_{\rm phase}$ might not be very useful. Indeed, $L_{\rm phase}$ does not mark the transition between the bar and the next component if their position angles are not more than 10° apart. This is the case in the direct and deprojected images of NGC 1211, and in the direct image of NGC 7280. In fact, Table 3 shows that $L_{\rm phase}$ is considerably bigger than $L_{\epsilon_{\min}}$ only in these galaxies. In NGC 1211, the oval disc has a position angle very similar to that of the bar, and in NGC 7280 the outer disc has a position angle similar to that of the bar. Hence, in these cases, the arbitrary 10° threshold that defines $L_{\rm phase}$ does not give a meaningful result, and one needs to search for a less conspicuous change in position angle that might indicate the transition between the components. A close inspection of the position angle radial profiles of NGC 1211 (Fig. 6) reveals glitches at 27 and 37 arcsec in the direct and deprojected measurements, respectively, and we will hereafter use these values as $L_{\rm phase}$. In the position angle radial profile of the direct image of NGC 7280, it is easy to note the transition between the bar and the outer disc starting at 21 arcsec from the centre, but it takes 11 arcsec more for this change to reach the threshold of 10° (see Fig. 10). Hence, in the following, we will use $L_{\rm phase} = 21$ arcsec for the direct image of NGC 7280. It is straightforward to verify that these values are a much better estimate of the bar-length in these galaxies than the values taken directly from the nominal definition of $L_{\rm phase}$.

The values of the bar-length in NGC 7743 quoted in Table 3 seem all to be excessively large in a comparison with the galaxy image in Figs 1 and 11. In particular, as mentioned in the last section, $L_{\epsilon_{\max}}$ seems to happen outside the bar, as a result of the smooth joining of the isophotes of the bar and the spiral arms. Erwin (2005) argues similarly. The other radial profiles also show smooth transitions. However, both the projected and deprojected ellipticity profiles have a small glitch at 33 and 35 arcsec from the centre, respectively. A comparison with the images argues that this glitch might be caused by the transition between the bar and the spiral arms, and so we choose its position as our fiducial value of the bar-length in this galaxy. This is in agreement with the estimates of Erwin (2005) that go from 31 to 37 arcsec. Nevertheless, since no glitches are present in the position angle profiles, we have to discard NGC 7743 in some of the analyses below.

Apart from NGC 7743, there are no published estimates of the bar-lengths of the galaxies in our sample. However, the values we obtain are of the same order as generally found in studies using optical images (see e.g. Erwin 2005; Gadotti & de Souza 2006, and references therein).

The two panels in Fig. 12 show that all measured scalelengths are strongly correlated. This is not surprising, since they refer to a specific structural component which is, for most of the points in these plots, the bar. These plots also include the oval discs measurements in NGC 266, NGC 1211 and NGC 7080, and the scalelengths of NGC 7743. Interestingly, these structures follow the same relation as the bars. This figure also shows that, as expected, $L_{b_4} < L_{\epsilon_{\max}}$. In Tables 3 and 4, one sees in fact that L_{b_4} is almost always the smallest value. In addition, it is interesting to note that $L_{{\rm prof}_i}$ is usually similar to L_{b_4}. Note also that the spread in the correlations is larger in the deprojected measurements, most likely due to the uncertainties in image deprojection.

In order to compare the results of the various methods to determine the bar-length, we need to use one of the characteristic lengths as an yard-stick. As discussed above, L_{b_4} is considerably smaller than the bar-length, while $L_{\rm drop}$, $L_{{\rm prof}_i}$ and $L_{{\rm prof}_f}$ are not meaningful for MD bars, and $L_{\epsilon_{\max}}$ is not meaningful for MH bars. This leaves $L_{\rm phase}$ and $L_{\epsilon_{\min}}$. We arbitrarily choose the former and give the results of the bar-length relative to this measure in Tables 5 and 6 for observed and deprojected images, respectively. Note that, since these are scalelength ratios, defined on the same position angle, one can work directly with the values from the projected images, assuming that these ratios do not change in the deprojected images. In fact, since the values in Tables 5 and 6 depict similar trends, we can carry on with our analysis using only the data in Table 5. The fact that there are a few differences means that image deprojection might sometimes modify the various scalelengths by

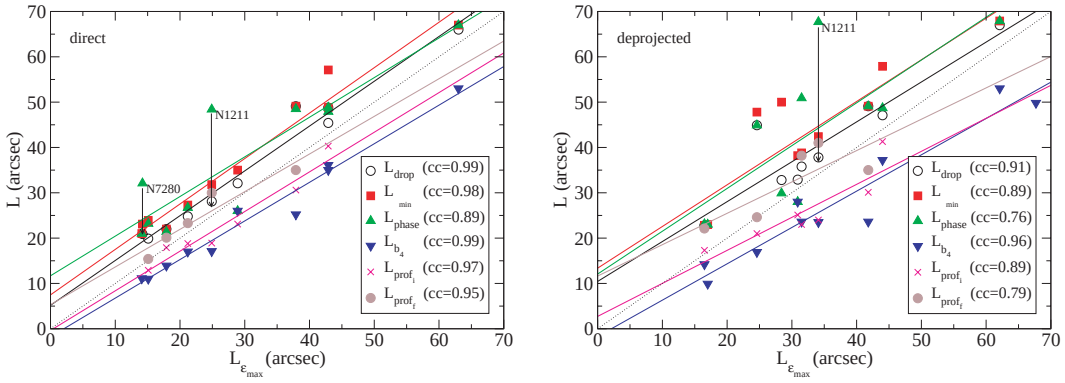

Figure 12. Correlation between all measured scalelengths in direct (left-hand panel) and deprojected images (right-hand panel), using $L_{\epsilon_{\rm max}}$ as a reference. The solid lines are linear fits to the data, for each scalelength separately, colour-coded as indicated. The dotted line is a one-to-one correspondence line. The arrows indicate our new definitions of $L_{\rm phase}$ for NGC 1211 and NGC 7280. Correlation coefficients are also shown. As expected, all scalelengths are clearly correlated. Note also that the uncertainties in image deprojection rise the spread in the correlations.

Table 5. Estimates for bar-lengths from direct images normalized by $L_{\rm phase}$.

Galaxy	$L_{\epsilon_{\rm max}}$	$L_{\rm drop}$	$L_{\epsilon_{\rm min}}$	L_{b_4}	$L_{{\rm prof}_i}$	$L_{{\rm prof}_f}$
N266	0.78	1.01	1.01	0.52	0.63	0.72
N357	0.80	0.93	1.02	0.64	0.70	0.87
N799	0.67	...	1.00	0.53	...	...
N1211	0.92	1.04	1.18	0.63	0.67	1.11
N1358	0.65	0.99	1.04	0.48	0.56	0.66
N7080	0.84	1.03	1.03	0.65	0.84	0.94
N7280	0.68	1.00	1.10	...	...	...

Notes. The same as Table 3 but with all measurements normalized by $L_{\rm phase}$.

Table 6. Estimates for bar-lengths from deprojected images normalized by $L_{\rm phase}$.

Galaxy	$L_{\epsilon_{\rm max}}$	$L_{\rm drop}$	$L_{\epsilon_{\rm min}}$	L_{b_4}	$L_{{\rm prof}_i}$	$L_{{\rm prof}_f}$
N266	0.85	1.00	1.00	0.48	0.63	0.71
N357	0.62	0.70	0.76	0.46	0.45	0.75
N799	0.74	...	1.00	0.43	...	...
N1211	0.92	1.02	1.15	0.63	0.65	1.11
N1358	0.55	1.00	1.07	0.38	0.47	0.55
N7080	0.84	0.99	0.99	0.61	0.75	0.96
N7280	0.95	1.10	1.68	...	...	...

Notes. The same as Table 5 but for the deprojected images.

different factors. To assess whether these differences are spurious, or not, one has to consider the morphology of each component in the galaxy and its true position in space with respect to the plane of the sky. This is beyond our present scope. Note that, for NGC 1211 and NGC 7280, the values of $L_{\rm phase}$ used in Tables 5 and 6 are not the nominal ones, as in Tables 3 and 4, but those defined and discussed above after a closer inspection of the position angle radial profiles.

Let us now compare the values of the various scalelengths as given by Table 5, that is, after scaling with $L_{\rm phase}$. The smallest one is clearly L_{b_4}, with a mean value of 0.58 ± 0.07. By definition, this quantity is expected to be smaller than the bar-length, since the maximum of b_4 should occur in the part dominated by the bulge, not at the end of the bar. $L_{{\rm prof}_i}$ is the second smallest scalelength, with a mean value of 0.68 ± 0.1. As already discussed, $L_{\epsilon_{\rm max}}$ is meaningful for MD-type bars, for which we find a mean value of 0.68; there are, however, only two such galaxies for which we could do this analysis. If we include the MH types in the statistics, we find 0.76 ± 0.1, but in many cases this value is ill defined. $L_{{\rm prof}_f}$ comes next, with a mean value of 0.86 ± 0.18. As expected, because this is a difficult measurement, the standard deviation is larger than that for other scalelength measurements. None the less, it gives an estimate closer to $L_{\rm phase}$ than the one given by $L_{{\rm prof}_i}$ and is in fact consistent with it to within the errors. We are left with two scalelengths, $L_{\epsilon_{\rm min}}$ and $L_{\rm drop}$. The latter is well defined only for MH types, for which we get a value of 1.00 ± 0.04. This value hardly changes if we add the one MD-type galaxy for which this measurement is possible. For $L_{\epsilon_{\rm min}}$ we get a mean value of 1.05 with a standard deviation of 0.06. Our measurements thus show that four determinations – namely $L_{\rm phase}$, $L_{\epsilon_{\rm min}}$, $L_{\rm drop}$ and to a lesser extent $L_{{\rm prof}_f}$ – give values which are equal within the errors. Although our result needs to be confirmed both with a larger observational sample and with a sample of *N*-body bars, it is tempting to conclude that these four determinations, or their average, should allow a fair measurement of the bar-length.

None the less, as we already noted above, $L_{\rm drop}$ coincides with the position where the minimum in b_4 happens. In fact, in all cases where this could be defined, that is, the MH-type bars, both radii are identical. This holds for projected and deprojected measurements. The only exception occurs in the deprojected image of NGC 1358, but below we will show evidences that suggest that the deprojected measurements for this galaxy might be to some extent affected by uncertainties in its values of i and $\rm PA_{ln}$. Since the position of the minimum in b_4 is the position where the bar reaches its maximum boxyness, this argues strongly in favour of $L_{\rm drop}$ to define the end of the bar, in particular because b_4 reaches zero very quickly after that.

6.2 Analytically deprojected bar-lengths

Because of image stretching, the use of deprojected images to obtain deprojected bar-lengths is subject to spurious geometric effects and errors, in particular if the inclination angle is large. However, theoretical studies on the orbital structure of barred galaxies and *N*-body simulations predict that the inner parts of bars might be vertically thick but the outer parts of bars are vertically thin (see Athanassoula 2005b). This structure was confirmed for our own galaxy (López-Corredoira et al. 2007, and references therein), for

Table 7. Results from the analytical deprojection of bars.

	N266[a]	N357[a]	N799[b]	N1211[a]	N1358[a]	N7080[a]	N7280[b]	N7743[c]
				2D				
Bar-length (arcsec)	50.0	34.8	24.3	38.3	36.4	23.3	24.5	33.8
Bar-length (kpc)	16.5	5.7	9.8	8.3	9.9	8.1	3.3	4.0
Ellipticity	0.59	0.58	0.41	0.60	0.58	0.59	0.21	0.38
$PA_{ln} - PA_{bar}$ (°)	51	84	66	72	77	76	62	−27
				1D				
Bar-length (arcsec)	49.9	34.7	24.1	37.9	35.5	23.3	21.9	33.7
Bar-length (kpc)	16.5	5.7	9.7	8.2	9.6	8.0	2.9	4.0

[a]$L_p = L_{drop}$.[b]$L_p = L_{phase}$.[c]L_p is taken as the position of the glitch in the ellipticity profile (see Section 6.1).

M31 (Athanassoula & Beaton 2006, see also Athanassoula 2006) and for a sample of 30 edge-on disc galaxies observed in the NIR (Bureau et al. 2006). If this is generally confirmed, then by knowing the inclination angle of the galaxy, and the position angles of the bar and of the line of nodes, one can obtain an analytical expression for the true bar-length from its projected size. This would work in the majority of cases; the only exceptions being near edge-on galaxies, or highly inclined galaxies with the bar major axis near the galaxy minor axis. In such cases and if the vertical extent of the inner part of the bar is sufficient, it could block the end of the bar from our view, so that both image and analytical deprojections would overestimate the bar-length.

We can first assume that a bar can be treated as a line and call this assumption our 1D approximation. Thus, with simple trigonometry arguments, it is straightforward to show that the true, deprojected length of the bar is given by

$$L_{bar} = L_p(\sin^2\alpha\ \sec^2 i + \cos^2\alpha)^{1/2}, \quad (1)$$

where L_p is the observed, projected bar-length, measured as, for example, L_{drop}, α is the difference between the position angle of the line of nodes and the position angle of the bar, and i is the inclination angle (see also Martin 1995). As expected, a bar parallel to the line of nodes shows always its true length, regardless of the inclination angle. Of course, this equation diverges when i reaches 90°, that is, in the case of perfectly edge-on galaxies.

However, bars are not thin lines and so it is unclear whether our 1D approximation holds for real bars, especially those which are not very narrow. Thus, in Appendix A, we derive expressions for the deprojected semimajor and semiminor axes, as well as position angle, of an ellipse seen in projection. This allows us to obtain analytically measurements of the lengths, ellipticities and position angles of the deprojected bars in our galaxies, taking into account the 2D properties of the bars.[2]

We calculated L_{bar} using equation (1) and the expressions from our 2D treatment and show the results in Table 7. The adopted values of the inclination angle, position angle of the line of nodes and α are taken from Table 1, whereas the values for the position angle of the bar and L_p are those extracted from our images. We used $L_p = L_{drop}$ for our MH-type galaxies and $L_p = L_{phase}$ for our MD-type galaxies, for which L_{drop} is not defined. The 1D and 2D deprojected bar-lengths agree very well with each other if the inclination is not too high. However, since the 1D approximation does not consider changes in the position angle, the values it provides for the bar-length are always slightly smaller. Table 7 also shows the deprojected ellipticities and position angles obtained with the 2D analysis. Comparing them with what is obtained from the deprojected images in Figs 3–11 one sees very good agreement. This means that the expressions in Appendix A can be reliably used to obtain deprojected ellipticities and position angles.

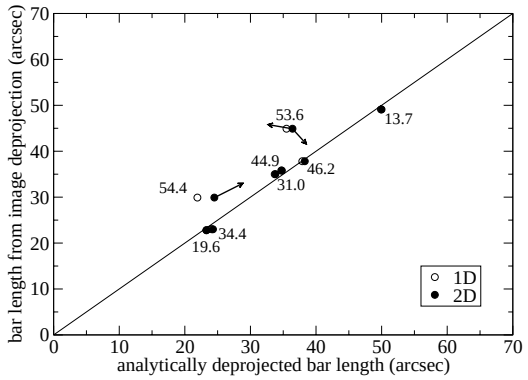

Figure 13. The true bar-length as measured from the deprojected images plotted against the same quantity as estimated analytically. The empty circles refer to our 1D approximation while the filled circles correspond to the equations derived in Appendix A in the 2D analytical treatment. The inclination angle i of each galaxy from Table 1 is written next to the corresponding points, and the solid line depicts a one-to-one correspondence. The arrows indicate values for NGC 1358 and NGC 7280 assuming an uncertainty of ±20° in PA_{ln}. In these cases, which are the most-inclined galaxies in our sample, the discrepancy between the results from the 2D analytical treatment and the deprojected images is alleviated if the true $PA_{ln} = 35°$ for the former and $PA_{ln} = 98°$ for the latter. Note that assuming for the latter a value for $PA_{ln} = 58°$ produces only a very weak oval whose length is not clearly discernible in the radial profiles from ellipse fits. This plot shows clearly that reliable estimates for the bar-length can be obtained analytically.

In Fig. 13, we show that L_{bar} from both the 1D and 2D analyses agree very well with each other and also with estimates from deprojected images, but only when the inclination angle is smaller than about 50°. Two of our galaxies do not satisfy this criterion: NGC 1358 and NGC 7280; the length of their bars, as estimated

[2] The source code of a FORTRAN program to perform these calculations can be downloaded from http://www.mpa-garching.mpg.de/∼dimitri/deprojell.f.

from deprojected images, is overestimated by 8.5 and 5.4 arcsec, respectively, that is, ≈ 20 per cent in both cases. Let us examine closer these two exceptional cases. How sure are we that the inclination angles we applied are correct? For NGC 1358, this parameter, as quoted in the literature, ranges from 37° to 55° (see results in NED and LEDA). Our choice is closer to the latter value and the ellipticity profile of the deprojected image argues in favour of it, as the ellipticity is close to zero in the outer parts (Fig. 7). To be reassured of that, we created a deprojected image of NGC 1358 assuming that $i = 40°$ and found that the disc remains significantly eccentric, again arguing that the true inclination angle of this galaxy is closer to 50° than to 40°. Thus, although a smaller inclination angle can alleviate the discrepancy in the bar-length estimates, we believe that our adopted values are more correct. For NGC 7280, the values of i in the literature range from 44° to 59°. We chose a value closer to the latter and again a similar analysis as done with NGC 1358 favours our choice. None the less, the wide range of estimates seen in the literature is an indication of how difficult and uncertain the measurement of i can be.

Alternatively, this discrepancy could be the result of an uncertainty of $\pm$ 20° in $\mathrm{PA_{ln}}$. As depicted by the arrows in Fig. 13, if the real position angle was 35° the difference in the case of NGC 1358 could be considerably alleviated. Similarly, the difference is less pronounced in the case of NGC 7280 if we add 20° to $\mathrm{PA_{ln}}$. Note, however, that assuming for the latter a value for $\mathrm{PA_{ln}} = 58°$ (i.e. 20° less than our original estimate) produces in the deprojected image only a very weak oval, whose length is not clearly discernible in the radial profiles from ellipse fits. To summarize, we do not believe that the discrepancies are due to erroneous choices of the viewing angles, but due to the difficulty in obtaining a correct deprojected image in cases that the inclination angle is considerable. Nevertheless, a larger sample is necessary to study this issue more thoroughly.

These results show that the deprojected length of bars can be reliably determined analytically, with no need of using deprojected images. Furthermore, the fact that the analytical expressions hold so well means that the assumption that the outer parts of bars are vertically thin (as opposed to their inner parts), as predicted by orbital structure work and by simulations, is correct. Indeed, if the ends of the bar were thick, the image and analytical deprojections would be significantly discrepant, and Fig. 13 shows that this is not the case, not even, in a clear way, for our two most inclined galaxies.

Using the results from our 2D analysis, one sees that, as expected from the results of the *N*-body simulations in AM02, MH-like galaxies have longer bars on average than MD-like galaxies: the median values are, respectively, 8.3 and 4.0 kpc. Nevertheless, to establish this difference fully, with a better statistical weight, we would need a bigger sample, particularly for MD-type bars.

7 DISCUSSION

7.1 The effects of deprojecting images

A deprojected image of an inclined galaxy is necessarily approximate, unless the inclination angle is negligible and/or the galaxy is razor thin. Indeed, one has to take into account the complete geometry of the different galaxy components, including the vertical properties of bulges, discs and bars, and these are not known exactly. For instance, since we do not know exactly the geometry of the bulge, in particular its vertical mass distribution and its orientation with respect to the disc, the stretching performed to generate the deprojected image might produce spurious effects in the bulge region, especially in the case of galaxies with massive bulges. One possible solution to this problem, proposed by, for example, Laurikainen et al. (2004), is to obtain a model for the bulge, remove it from the image, and put it back *after* deprojection. Yet this approach is not flawless either since it assumes that the bulge mass distribution is spherically symmetric. We prefer to give the results from deprojected images as indicative only. In a future paper, when we compare our results to *N*-body bars we will project the *N*-body snapshots rather than using results from deprojected images.

Nevertheless, deprojected measurements have been used in the literature and thus it is interesting to examine the changes introduced in the galaxy images by deprojection (see also Jungwiert, Combes & Axon 1997). One sees in Figs 3–11 that, when i is smaller than about 30°, projected and deprojected images are very similar. Thus, let us now focus our analysis on galaxies with i larger than about 30°. One sees that the position of the plateau/peak in ellipticity in their deprojected images moves outwards in all cases, indicating longer bars. This is expected since, unless the bar is aligned parallel to the line of nodes, the bar-length will always be shortened by projection. In most cases, the maximum in ellipticity occurs at higher ellipticity values, meaning more eccentric bars. This of course is due to the fact that the position angle of the bar is nearer to perpendicular to the galaxy major axis than along it. On the contrary, in NGC 7280 the peak in ellipticity occurs at lower values when the image is deprojected, because the position angle of the bar is closer to the galaxy major axis. Similar arguments can be applied to L_{b_4}, clearly defined for MH-type galaxies, which also moves outwards, while the value of b_4 peak itself is lowered when projection effects are considered.

The effects of deprojection on the brightness profiles are also clear. As expected, the isophotes reach larger distances. In addition, the breaks where the bar ends consistently move outwards and might also look milder. This is a result of the amplification of the image in the direction perpendicular to the line of nodes. Furthermore, there are changes in the surface brightness levels proper, in particular in the centre, to account for the fact that the area on the sky comprised by the galaxy is larger in the deprojected image. This highlights the importance of performing a flux-conserving stretching of the image during deprojection.

Deprojecting the images has also interesting effects on the position angle radial profiles. In NGC 357, one sees that the outer change in position angle due to the ring practically disappears. The line of nodes lies roughly along the position angle of the ring, which is then stretched along the perpendicular direction. The result is that from being almost perpendicular to the bar, the ring becomes almost parallel. This is interesting since both simulations (Schwarz 1979, 1981) and analysis of observations (Buta 1986, 1995) show that inner rings are preferentially aligned with bars. Thus, at least part of those which are not seen parallel might be in fact a result from projection effects. Since the ring in the deprojected image is close to circular, the position angle profile is very noisy in this region. Note also that the difference between the position angle of the bar and the line of nodes is always larger when the galaxy is deprojected.

7.2 Comparing real and *N*-body bars

Obviously, a successful modelling of the origin and evolution of bars in galaxies has to provide bars with properties that match those of real barred galaxies. Conversely, the observation of bars with different properties, when linked to theoretical studies, may provide clues to explain the observed diversity. The analysis we present in this paper suggests a number of useful comparisons to *N*-body realizations of barred galaxies. An example of how useful such

comparisons may be can be seen in Gadotti & de Souza (2003) where, for instance, the ellipticity profile is used to evaluate how different *N*-body models compare to a real galaxy.

From the behaviour of the radial profiles of ellipticity presented here, one is able to distinguish cases which are similar to one of the prototypical models in AM02. The weak bars in NGC 799 and NGC 7280 share a similar ellipticity profile (*with a gentle drop after the bar*) with their MD models, which indeed produce weak bars as a result of the limited bar–halo interaction. On the other hand, the *steep drop* in ellipticity seen in our strong bars (in particular, NGC 266, NGC 1211 and NGC 7080) is a property of the MH models, that form the strongest bars from the vigorous bar–halo interaction. Therefore, the abruptness of this drop seems to be a useful indicator to separate real instances of the MH and MD cases.

One also expects the models to explain the observed lengths of bars. The lengths of bars, in connection to their ellipticities and Fourier even components, are related to their strength and importance in the overall evolution of the galaxy. Other studies suggest in addition that bars can get longer during the course of their evolution (Athanassoula 2003), which is also in agreement with recent observational results (Gadotti & de Souza 2005, 2006). This adds relevance, but also complexity, to a comparison between the lengths of observed and simulated bars. Here we aimed at the first step of this comparison, namely how to measure the bar-length.

We postpone to a future paper a more thorough comparison between the observed properties presented here and those obtained in a similar way from snapshots of *N*-body realizations.

8 SUMMARY AND CONCLUDING REMARKS

In this paper, we made a thorough analysis of morphological and photometrical properties of a sample of barred galaxies, to be compared in future work to the corresponding properties of bars in *N*-body simulations. Our sample is relatively small, of nine galaxies, but this has proven to be an asset since it allowed us to examine each case separately, in depth, without having to rely on an automatic treatment. This became particularly clear when we worked on the scalelengths. The difficulty in measuring the bar-length highlights the necessity of inspecting each case individually and making judgements which no automated approach could make. This was possible here only due to the relatively restricted size of our sample.

We have used two NIR wavelengths, so that we can follow the properties of the old stellar population, which contributes most of the visible matter. Surface brightness radial profiles, obtained either from cuts along the bar major and minor axes, as well as globally over the surface of the galaxy, allowed us to study the light distribution and the sharp drops at the end of the bar. We also made radial profiles of the colour, position angle, ellipticity and shape. We found that there are universal formats for the latter two, linked to the form and properties of the bar. In particular, we find that five of our galaxies have profiles such as those of MH-type *N*-body bars (AM02), that is, a high axial ratio, near-constant within a considerable radial region, followed by a very steep drop. The corresponding b_4 profiles showed the existence of strong rectangular-like shapes. All these, taken together, suggest that a considerable amount of angular momentum has been exchanged within these galaxies, that is, their haloes have resonances that are capable of absorbing considerable amounts of angular momentum (Athanassoula 2003). On the other hand, three of our galaxies have MD-type characteristics, namely an ellipticity profile with a maximum at low values and no sharp drop, and very low values of the b_4. We believe that the halo of these galaxies has been able to exchange considerably less angular momentum than in the previous cases. These first results will be followed by a thorough comparison with *N*-body bars, to gauge better the halo properties, the angular momentum exchange and its effect on bar growth and slow-down.

We have also measured several characteristic scalelengths. The peaks of b_4 and of the ellipticity are at a radius well within the bar. This is likewise true for the end of the ledges on the radial photometric profiles due to the bar (L_{prof_i}). The radius at which the bump in the luminosity profile due to the bar smoothly joins up to the disc profile (L_{prof_f}) is closer to the end of the bar, but usually difficult to determine. We found four scalelengths whose values roughly coincide, and which could be used to measure the bar-length, namely L_{phase}, L_{drop}, $L_{\epsilon_{\mathrm{min}}}$ and L_{prof_f}, although the measurements of the last one are much more noisy than those of the other three. Furthermore, we found that L_{drop} coincides with the position where the bar reaches its maximum boxyness, strongly arguing in favour of this scalelength being an accurate measurement of the bar-length in MH-type galaxies, where this drop is pronounced. None the less, it is important to have more than one such measure for two main reasons. First, in order to be able to make comparisons and averages to diminish the effect of uncertainties (AM02). Secondly, because according to the characteristics of the galaxy some of these measurements are not possible. We discussed in length some such cases here. The link of these scalelengths with the resonances will be made with the help of *N*-body bars elsewhere.

Simulations predict that MH-like bars should be longer than MD-like bars (AM02). Our measurements of the bar-length bear this prediction out. Indeed, we find that the median value for the bar-length in the MH sample is 8.3 kpc, compared to a median bar-length of 4 kpc for the MD galaxies.

The assumption that the outer part of the bar is vertically thin allowed us to obtain formulae for the deprojected bar-length, ellipticity and position angle. We have shown that these estimations agree very well with the values obtained from the deprojected image for all our galaxies where we consider the latter to be reliable. This confirms a theoretical prediction coming from both orbital structure theory and *N*-body simulations, namely that while the inner part of the bar might be vertically thick the outer part is vertically thin (Athanassoula 2005b). Since these are intrinsic properties of the bar, independent of our viewing angle, the values obtained from our formulae should be valid even for cases of highly inclined galaxies, where the deprojected image might not be reliable.

In a future paper, we will apply the same surface photometry techniques used here to a suitable sample of *N*-body simulations of barred galaxies, similar to those presented in AM02. We then intend to address whether or not a distinction between MH and MD bars can in fact be done in real galaxies as well, judging from a thorough comparison between the surface photometry results in both real galaxies and simulations, including different techniques of image decomposition (e.g. de Souza, Gadotti & dos Anjos 2004; Laurikainen, Salo & Buta 2005; Buta et al. 2006). If successful, this approach could allow us to obtain information on the halo component and on the angular momentum exchange within the galaxy directly from surface photometry and morphology. We will also include in our comparisons the vertical *kinematics* in observed and model bars, using, for example, the measurements of Gadotti & de Souza (2005).

ACKNOWLEDGMENTS

It is a pleasure to thank an anonymous referee for many useful comments and remarks and Raúl Mújica for his efforts, which made

this work possible. We also thank ECOS and ANUIES for financing the exchange project M04U01, and FAPESP for grants 03/07099-0 and 00/06695-0. DAG, EA and AB would like to thank INAOE for their kind hospitality, both in the Tonanzintla and the Cananea sites. DAG thanks the CNRS for a six-month poste rouge during which the data were analysed and the project started. DAG is supported by the Deutsche Forschungsgemeinschaft priority program 1177 ('Witnesses of Cosmic History: Formation and evolution of galaxies, black holes and their environment') and the Max Planck Society. CANICA was developed under CONACYT project G28586E (PI: L. Carrasco). This research has made use of NED, which is operated by the Jet Propulsion Laboratory, California Institute of Technology, under contract with the National Aeronautics and Space Administration. This research has also made use of NASA's Astrophysics Data System and of the HyperLeda data base (http://leda.univ-lyon1.fr/).

REFERENCES

Athanassoula E., 1992, MNRAS, 259, 328
Athanassoula E., 2002, ApJ, 569, L83
Athanassoula E., 2003, MNRAS, 341, 1179
Athanassoula E., 2005a, Celest. Mech. Dyn. Astron., 91, 9
Athanassoula E., 2005b, MNRAS, 358, 1477
Athanassoula E., 2005c, in Gottesman S. T., Buchler J.-R., eds, Nonlinear Dynamics in Astronomy and Physics (In memory of Henry E. Kandrup). Annals of the New York Academy of Sciences, 1045. New York, NY, p. 168
Athanassoula E., 2006, in Wada K., Combes F., eds, Mapping the Galaxy and Nearby Galaxies. In press (astro-ph/0610113)
Athanassoula E., 2007, MNRAS, 377, 1569
Athanassoula E., Beaton R. L., 2006, MNRAS, 370, 1499
Athanassoula E., Misiriotis A., 2002, MNRAS, 330, 35 (AM02)
Athanassoula E., Morin S., Wozniak H., Puy D., Pierce M. J., Lombard J., Bosma A., 1990, MNRAS, 245, 130
Berentzen I., Shlosman I., Jogee S., 2006, ApJ, 637, 582
Bureau M., Aronica G., Athanassoula E., Dettmar R.-J., Bosma A., Freeman K. C., 2006, MNRAS, 370, 753
Bureau M., Athanassoula E., 2005, ApJ, 626, 159
Bureau M., Freeman K. C., 1999, AJ, 118, 126
Buta R., 1986, ApJS, 61, 609
Buta R., 1995, ApJS, 96, 39
Buta R., Vasylyev S., Salo H., Laurikainen E., 2005, AJ, 130, 506
Buta R., Laurikainen E., Salo H., Block D. L., Knapen J. H., 2006, AJ, 132, 1859
Cole S., Lacey C., 1996, MNRAS, 281, 716
Colin P., Valenzuela O., Klypin A., 2006, ApJ, 644, 687
Curir A., Mazzei P., 1999, A&A, 352, 103
de Souza R. E., dos Anjos S., 1987, A&AS, 70, 465
de Souza R. E., Gadotti D. A., dos Anjos S., 2004, ApJS, 153, 411
de Vaucouleurs G., de Vaucouleurs A., Corwin H. G., Buta R. J., Paturel G., Fouque P., 1991, Third Reference Catalog of Bright Galaxies. Springer-Verlag, New York (RC3)
Ebneter K., Davis M., Djorgovski S., 1988, AJ, 95, 422
Elmegreen B. G., Elmegreen D. M., 1985, ApJ, 288, 438
El-Zant A., Shlosman I., 2002, ApJ, 577, 626
Erwin P., 2004, A&A, 415, 941
Erwin P., 2005, MNRAS, 364, 283
Erwin P., Sparke L., 2002, AJ, 124, 65
Erwin P., Sparke L., 2003, ApJS, 146, 299
Freeman K. C., 1970, ApJ, 160, 811
Gadotti D. A., 2003, PhD thesis, University of São Paulo
Gadotti D. A., de Souza R. E., 2003, ApJ, 583, L75
Gadotti D. A., de Souza R. E., 2005, ApJ, 629, 797
Gadotti D. A., de Souza R. E., 2006, ApJS, 163, 270
Gadotti D. A., dos Anjos S., 2001, AJ, 122, 1298
Hayashi E., Navarro J. F., Springel V., 2007, MNRAS, 377, 50
Heller C. H., Shlosman I., Athanassoula E., 2007, ApJ, 657, L65
Hunt L. K., Mannucci F., Testi L., Migliorini S., Stanga R. M., Baffa C., Lisi F., Vanzi L., 1998, AJ, 115, 2594
Jedrzejewski R. I., 1987, MNRAS, 226, 747
Jungwiert B., Combes F., Axon D. J., 1997, A&AS, 125, 479
Kormendy J., 1979, ApJ, 227, 714
Kormendy J., Kennicutt R. C., 2004, ARA&A, 42, 603
Kuijken K., Merrifield M. R., 1995, ApJ, 443, L13
Laurikainen E., Salo H., Buta R., Vasylyev S., 2004, MNRAS, 355, 1251
Laurikainen E., Salo H., Buta R., 2005, MNRAS, 362, 1319
Laurikainen E., Salo H., Buta R., Knapen J. H., Speltincx T., Block D. L., 2006, AJ, 132, 2634
López-Corredoira M., Cabrera-Lavers A., Mahoney T. J., Hammersley P. L., Garzòn F., Gonzalez-Fernandez C., 2007, AJ, 133, 154
Ma J., Peng Q., Gu Q.-S., 1998, A&AS, 130, 449
Marinova I., Jogee S., 2007, ApJ, 659, 1176
Martin P., 1995, AJ, 109, 2428
Martinez-Valpuesta I., Shlosman I., Heller C., 2006, ApJ, 637, 214
Menendez-Delmestre K., Sheth K., Schinnerer E., Jarrett T. H., Scoville N. Z., 2007, ApJ, 657, 790
Michel-Dansac L., Wozniak H., 2006, A&A, 452, 97
Ohta K., Hamabe M., Wakamatsu, K-I., 1990, ApJ, 357, 71
O'Neill J. K., Dubinski J., 2003, MNRAS, 346, 251
Patsis P. A., Skokos C., Athanassoula E., 2003, MNRAS, 342, 69
Sandage A., Tammann G. A., 1981, A Revised Shapley-Ames Catalog of Bright Galaxies. Carnegie Institution, Washington
Schwarz M. P., 1979, PhD thesis, ANU
Schwarz M. P., 1981, ApJ, 247, 77

APPENDIX A: ANALYTICAL DEPROJECTION OF AN ELLIPSE

In the following, we will derive analytical expressions for the true semimajor and semiminor axes and position angle of an ellipse seen in projection.[3]

In the reference frame of an ellipse, that is, in a coordinate system (s, t) centred at the ellipse centre and with the axis of the abscissae s aligned with the ellipse major axis, one can write

$$\frac{s^2}{a^2} + \frac{t^2}{b^2} = 1, \tag{A1}$$

where a and b are the ellipse semimajor and semiminor axes. Considering a coordinate system (x, y), rotated with respect to the ellipse coordinate system but also centred at the ellipse centre, one can show that

$$\begin{aligned} s &= x\cos\alpha + y\sin\alpha, \\ t &= y\cos\alpha - x\sin\alpha, \end{aligned} \tag{A2}$$

where α is the angle between the two coordinate systems, counted counter-clockwise from (x, y) to (s, t). Substituting equation (A2) into equation (A1), it is possible to obtain the equation of the ellipse in the (x, y) coordinate system in its quadratic form

$$Ax^2 + 2Bxy + Cy^2 + 2Dx + 2Fy + G = 0, \tag{A3}$$

where

$$A = \frac{\cos^2\alpha}{a^2} + \frac{\sin^2\alpha}{b^2}, \tag{A4}$$

$$B = \frac{\cos\alpha\sin\alpha}{a^2} - \frac{\cos\alpha\sin\alpha}{b^2}, \tag{A5}$$

[3] The source code of a FORTRAN program to perform these calculations can be downloaded from http://www.mpa-garching.mpg.de/~dimitri/deprojell.f.

$$C = \frac{\sin^2\alpha}{a^2} + \frac{\cos^2\alpha}{b^2}, \tag{A6}$$

and $D = F = 0$ and $G = -1$.

Now, consider that the ellipse and its reference frame (s, t) are rotated about the x-axis by an angle i. The projection of the inclined ellipse on to the plane given by (x, y) gives another ellipse, whose equation is identical to equation (A3), except that y is replaced by $y \cos i$. It is straightforward to show that the equation of the deprojected ellipse is

$$A'x^2 + 2B'xy + C'y^2 + 2D'x + 2F'y + G' = 0, \tag{A7}$$

where

$$B' = B\cos i, \tag{A8}$$

$$C' = C\cos^2 i, \tag{A9}$$

and $A' = A, D' = F' = 0$ and $G' = G = -1$.

The semimajor and semiminor axes of an ellipse, as well as its position angle, can be directly obtained from its quadratic equation. For the deprojected ellipse,

$$s1 = \left\{\frac{2(A'F'^2 + C'D'^2 + G'B'^2 - 2B'D'F' - A'C'G')}{(B'^2 - A'C')[(C' - A')\sqrt{1 + 4B'^2/(A' - C')^2} - (C' + A')]}\right\}^{1/2} \tag{A10}$$

and

$$s2 = \left\{\frac{2(A'F'^2 + C'D'^2 + G'B'^2 - 2B'D'F' - A'C'G')}{(B'^2 - A'C')[(A' - C')\sqrt{1 + 4B'^2/(A' - C')^2} - (C' + A')]}\right\}^{1/2}, \tag{A11}$$

and the semimajor and semiminor axes are given, respectively, by $a' = \max(s1, s2)$ and $b' = \min(s1, s2)$. Thus, the ellipticity is $1 - b'/a'$.

The position angle of the deprojected ellipse is given by

$$\theta = -\frac{1}{2}\cot^{-1}\left(\frac{C' - A'}{2B'}\right) \tag{A12}$$

and counted counter-clockwise from the axis in (x, y) which is closer to the ellipse major axis.

Note that equations (A10) and (A11) have singularities when $i = 0$ and $\alpha = \pm n\pi/4$ (n being a positive integer). A singularity also appears in equation (A12) when $\alpha = 0, \pm n\pi/2$. If $i = \pi/2$, the above three equations diverge. For the practical purpose of obtaining deprojected measurements of the properties of galactic bars from ellipse fits, α is the angle between the bar and the line of nodes, and i is the galaxy inclination angle.

This paper has been typeset from a TEX/LATEX file prepared by the author.